

ELECTRON CHANNELING RADIATION FROM DIAMOND

R.K. Klein, J.O. Kephart, R.H. Pantell, H. Park
Stanford University
Stanford, CA 94305

B. L. Berman
University of California, LLNL
Livermore, CA 94550

R. L. Swent
Varian Associates
Palo Alto, CA 94303

S. Datz and R. W. Fearick
Oak Ridge National Laboratory
Oak Ridge, TN 37830

This paper was prepared for submittal to
Physical Review B

April 1984



Lawrence
Livermore
National
Laboratory

This is a preprint of a paper intended for publication in a journal or proceedings. Since changes may be made before publication, this preprint is made available with the understanding that it will not be cited or reproduced without the permission of the author.

DISCLAIMER

This document was prepared as an account of work sponsored by an agency of the United States Government. Neither the United States Government nor the University of California nor any of their employees, makes any warranty, express or implied, or assumes any legal liability or responsibility for the accuracy, completeness, or usefulness of any information, apparatus, product, or process disclosed, or represents that its use would not infringe privately owned rights. Reference herein to any specific commercial product, process, or service by trade name, trademark, manufacturer, or otherwise, does not necessarily constitute or imply its endorsement, recommendation, or favoring by the United States Government or the University of California. The views and opinions of authors expressed herein do not necessarily state or reflect those of the United States Government or the University of California, and shall not be used for advertising or product endorsement purposes.

ELECTRON CHANNELING RADIATION FROM DIAMOND

R.K. Klein, J.O. Kephart, R.H. Pantell, and H. Park
Department of Electrical Engineering
Stanford University
Stanford, CA 94305

B. L. Berman
Lawrence Livermore National Laboratory
University of California
Livermore, CA 94550

R.L. Swent
Varian Associates
Palo Alto, CA 94303

S. Datz and R.W. Fearick*
Oak Ridge National Laboratory
Oak Ridge, TN 37830

A series of channeling-radiation experiments for incident electrons of 16.9, 30.5, and 54.5 MeV has been performed, using a type-IIa natural diamond 23 μm thick. Channeling-radiation transition energies calculated with the standard (Hartree-Fock) potential are in good agreement with the observed results for the (100) and (110) planes as well as for the $\langle 100 \rangle$ axis at all energies, but are in error for the (111) plane. Corrections to the (111) potential due to anisotropic electron distributions which are based upon x-ray-diffraction data result in calculated transition energies that are in better agreement with the observed data; an empirical (111) potential yields calculated transition energies which are in even better agreement with the data. Calculated linewidths are considerably narrower than the observed values; this disagreement probably results from incoherent scattering by crystal defects having an average spacing of approximately 1 μm . The transition energies are shown to scale as $\gamma^{5/3}$ for transitions involving states that are localized close to the atomic planes and as γ^2 for those localized close to the midplane regions. Free-state populations are shown to increase relative to bound-state populations with incident electron-beam energy. Channeling radiation has been shown to constitute a practical source of x-ray photons utilizable at many existing accelerators.

PACS numbers: 61.80.Mk, 41.70.+t, 78.70.-g, 61.70.-r

*Permanent address: University of the Witwatersrand, Johannesburg 2001, South Africa

I. INTRODUCTION

In this paper we report observations of channeling radiation from electrons incident along the axes and planes of a diamond crystal at electron energies of 16.9, 30.5, and 54.5 MeV. In addition, the experimental and calculational methods used by our group are described in some detail. Finally, an analysis of the suitability of channeling radiation from such a crystal as a useful source of x-rays is carried out.

Channeling radiation is produced when relativistic charged particles such as electrons or positrons enter a crystal along a direction that is very close to one of high symmetry (an axis or a plane), and are channeled along that direction. Quantum-mechanically, the charged particle can be considered to be bound by the transverse electrostatic potential of the crystal axis or plane, and channeling radiation occurs as spontaneous transitions between eigenstates of this potential. In the longitudinal rest frame of the electron, these transitions have energies on the order of hundreds of eV, but in the laboratory frame there is a relativistic (Doppler) increase in the emitted photon energy by a factor of 2γ , where γ is the ratio of particle energy to rest energy. For the electron energies of our experiments, channeling radiation is observed in the energy region from tens to hundreds of keV.

Channeling radiation has several interesting and potentially very useful characteristics: it is bright--often more than an order of magnitude brighter than bremsstrahlung; it is of narrow linewidth in the spectral peaks; and it is forward-directed with an angle of emission $\theta \lesssim 1/\gamma$. Also, the channeling radiation from planar-channeled electrons is linearly polarized in the direction perpendicular to the channeling plane, while that from axially channeled electrons has a component of linear polarization when the

incident beam is directed at a nonzero angle with respect to the channeling axis. In addition, because the channeling radiation has the same time structure as the incident electron beam, which can be bunched in pulses as narrow as several picoseconds, the pulse of radiation can be of extremely short duration. These qualities make channeling radiation a unique photon source in much of the x-ray spectral region.

Diamond is an eminently suitable crystal to use for channeling-radiation experimental studies because of its low Z and because its very high Debye temperature (~ 2000 K) results in a small one-dimensional rms thermal-vibration amplitude (0.042 Å), about half that of silicon (0.075 Å). This latter property is important because channeling-radiation linewidths are strongly dependent upon the lifetimes of the initial and final eigenstates, which are shortened by thermal incoherent scattering. Diamond does, however, suffer from the drawback that typical crystal quality is much poorer than that of silicon, for example, for which essentially perfect crystals are readily available. Observations of electron channeling radiation for diamond have been reported previously for electrons of a few MeV,¹ ≈ 54 MeV,²⁻⁴ and in the GeV energy region.^{5,6}

II. THEORETICAL CALCULATIONS

A. Energy Levels

Channeling-radiation transition energies are computed by solving a many-beam formulation of the Schrödinger equation

$$[|\vec{p}|^2/2m\gamma + V(\vec{r})] \chi(\vec{r}) = E \chi(\vec{r}) \quad (1)$$

where \vec{p} and m are the momentum and rest mass of the particle, E is its energy, $\chi(\vec{r})$ is the wave function associated with the particle, and $V(\vec{r})$ is the potential function in the laboratory frame. The Schrödinger equation (rather than the Dirac equation) is used here for describing the motion of the electron along the transverse coordinate \vec{r} because the transverse motion is nonrelativistic; that is, the depth of the potential well in the rest frame of the electron (γV) is much smaller than its rest mass. Of course it can be shown that the Dirac equation reduces to the Schrödinger equation under these conditions. The many-beam formulation was first utilized with reference to channeling phenomena by Andersen et al.⁷ (This approach is similar to the plane-wave expansion for electronic energy levels in crystals.) In this formulation it is recognized that the lattice potential is periodic and can be expanded as a Fourier series, so that in the axial case

$$V(\vec{r}) = \sum_{\vec{n}} v_{\vec{g}_n} e^{i\vec{g}_n \cdot \vec{r}} \quad (2)$$

where the \vec{g}_n 's represent transverse reciprocal lattice vectors and the summation is over all of these vectors. In the planar case, the above equation simplifies because $\vec{r} \rightarrow x$ always is taken to be normal to the plane and $\vec{g} \rightarrow g$ is the reciprocal lattice vector normal to the plane, so that the planar potential can be written as

$$V(x) = \sum_n v_n e^{ingx} \quad [n = \dots, -1, 0, 1, 2, \dots] \quad . \quad (3)$$

In both cases, the sums are truncated after a finite number of terms ("beams") for computational purposes.

The eigenfunctions are two-dimensional (axial case) or one-dimensional (planar case) Bloch functions of the form

$$\chi(\vec{r}) = \frac{1}{\sqrt{S}} e^{i\vec{k}_t \cdot \vec{r}} \sum_n c_n e^{i\vec{g}_n \cdot \vec{r}} \quad (\text{axial}) \quad \text{or} \quad (4)$$

$$\chi(x) = \frac{1}{\sqrt{L}} e^{ikx} \sum_n c_n e^{ingx} \quad (\text{planar}) \quad (5)$$

where S and L are the respective normalization area and length, and \vec{k}_t and k are momentum vectors lying in the first Brillouin zone.

When the above expressions are substituted into Eq. (1), the problem of solving for the energy eigenvalues and wave functions reduces to finding the eigenvalues of a (sometimes large) matrix A , whose components for the axial case are

$$A_{nm} = v(\vec{g}_n - \vec{g}_m) \quad (\text{for } n \neq m) \quad \text{and} \quad (6)$$

$$A_{nn} = \frac{\hbar^2}{2m\gamma} |\vec{k}_t + \vec{g}_n|^2 + v_0 \quad (7)$$

and for the planar case are

$$A_{nm} = v_{(n-m)} \quad (\text{for } n \neq m) \quad \text{and} \quad (8)$$

$$A_{nn} = \frac{\hbar^2}{2m\gamma} (k + ng)^2 + v_0 \quad . \quad (9)$$

The Fourier components $v_{\vec{g}_n}$ or v_n can be computed conveniently from tabulated electron scattering factors $f_e(s)$ which are proportional to the Fourier transforms of the potential. These scattering factors are defined as

$$f_e(s) = \frac{2me}{\hbar^2} \int_0^\infty r^2 V(r) \frac{\sin(4\pi sr)}{4\pi sr} dr \quad (10)$$

where $V(r)$ is the atomic potential and $4\pi s$ is the change in the magnitude of the wave vector of the electron in a scattering event. Analysis shows that the Fourier components can be written for the axial case as

$$v_{\vec{g}_n} = \frac{S_{\vec{g}_n} \hbar^2}{2\pi m} f_e \left\{ \frac{|\vec{g}_n|}{4\pi} \right\} \quad (11)$$

and for the planar case as

$$v_n = \frac{S_n \hbar^2}{2\pi m} f_e \left\{ \frac{ng}{4\pi} \right\} \quad (12)$$

Here $S_{\vec{g}_n}$ or S_n is the structure factor for the particular reciprocal lattice vector, defined for a single-element crystal as

$$S_{\vec{g}_n} = \frac{1}{V_c} \sum_j e^{i\vec{r}_j \cdot \vec{g}_n} \quad (13)$$

where V_c is the volume of the unit cell and \vec{r}_j are the coordinates of the atoms in the unit cell.

Near $r = 0$, the potential is smeared out by the thermal vibrations of the lattice. As is customary in the analysis of x-ray-diffraction data, we assume that this thermal smearing can be described by a convolution of the static potential with a Gaussian having a width equal to the thermal-vibration

amplitude. However, since the calculations are performed in reciprocal space, the convolution is much more easily accomplished: it consists of multiplying the Fourier coefficients by a Debye-Waller factor, defined for the axial case as

$$D_a = \exp\left[-\frac{1}{2} (\vec{g}_n | u_t)^2\right] \quad (14)$$

and for the planar case as

$$D_p = \exp\left[-\frac{1}{2} (ng_u)^2\right] \quad (15)$$

Here u_t is the two-dimensional rms vibrational amplitude, generally taken to be $\sqrt{2} u$, where u is the one-dimensional vibrational amplitude.

Clearly, the axial and planar calculations are very similar; with the identification $ng \rightarrow \vec{g}_n$ they are almost identical. However, for actual computation the planar case is much simpler, because it is only a one-dimensional problem, with just one transverse reciprocal lattice vector (and, of course, its multiples), thereby avoiding vector calculations.

The precision of these many-beam computations depends largely upon the number of reciprocal lattice vectors that one uses. For example, the simplest meaningful calculation for the axial case involves three reciprocal lattice vectors: the two basic reciprocal lattice vectors ($\vec{g}_{1,0}$ and $\vec{g}_{0,1}$) and the zero vector. We refer to this as a 3x3-beam calculation; as can be seen from Fig. 1(a), there are only nine linear combinations of these vectors, resulting in a 9x9 matrix to be solved.

For the planar case, by contrast, a 9x9 matrix, which we refer to as a 9-beam planar calculation, allows one to use vectors which reach considerably further into the reciprocal lattice, as can be seen from Fig. 1(b). Moreover, the potentials and eigenvalues converge much more slowly for the axial case

than for the planar one, although the magnitudes of the Fourier coefficients decrease with the magnitude of \vec{g} at about the same rate for both cases. This is because increasing the number of beams adds many more reciprocal lattice points (although with smaller Fourier coefficients) for the axial case than it does for the planar one. Hence for the axial case the high-magnitude reciprocal lattice points have a much larger effect than they do for the planar case, and the calculations converge much more slowly for the former than for the latter. This is purely a consequence of the one-dimensionality of the planar problem in contrast with the two-dimensionality of the axial problem, but it does mean that for a given amount of computing power the planar case can be calculated with considerably more precision. As an illustration, Fig. 2 shows how the potential converges with matrix size for the diamond $\langle 100 \rangle$ axis [Fig. 2(a)] and (100) plane [Fig. 2(b)]. The (100) planar potential is very well described by the 13-beam calculation (requiring the solution of only a 13x13 matrix), whereas the $\langle 100 \rangle$ axial potential still has not yet converged in the 11x11-beam calculation (already requiring the solution of a 121 x 121 matrix).

B. Selection Rules and Transition Strengths

Channeling radiation results when a channeled electron makes a transition between an initial eigenstate $|i\rangle$ and a final eigenstate $|f\rangle$; the emitted photon has energy $E_{fi} = (E_f - E_i)$. For a given spectral resonance, the integrated intensity is proportional to the transition strength. In the dipole approximation, the strength of a transition is proportional to the transition energy E_{fi} and to $|\langle \vec{p} \rangle|^2$ (see, e.g., Ref. 8), where $\langle \vec{p} \rangle = \langle f | \vec{p} | i \rangle$. The conditions on $|f\rangle$ and $|i\rangle$ in order that $\langle f | \vec{p} | i \rangle \neq 0$ are the selection rules of the system.

In the diamond crystal, a proper choice of origin leads to potentials which are symmetric with respect to a displacement coordinate \vec{r} ; that is, $V(\vec{r}) = V(-\vec{r})$. This in turn implies that each of the eigenfunctions $|i\rangle$ and $|f\rangle$ has a definite parity, odd or even.

For the planar case, the transverse potential is one-dimensional, and eigenfunctions can be characterized by a single quantum number n (plus the transverse wave vector k). As is shown in Fig. 3, the parity of the eigenfunctions (for $k = 0$) alternates from even to odd ($n = 0$ has even parity). For $k \neq 0$ the states do not have definite parity, but when there is no band structure they do, and this is very nearly the case for all tightly bound states.) Therefore, the matrix element $\langle f | \vec{p} | i \rangle$ is equal to zero unless the initial and final eigenstates have opposite parity -- in other words, unless Δn (between $|f\rangle$ and $|i\rangle$) is odd. Normally, the $\Delta n = 1$ transitions dominate the spectrum, but $\Delta n = 3$ transitions have been seen as well.⁹

For the axial case, the potential acting upon the more tightly bound electrons is almost cylindrically symmetric, and the eigenfunctions have an angular-momentum quantum number l in addition to the principal quantum

number n . Following common spectrographic notation, we label the angular-momentum states with $\ell = 0, 1, 2, 3, \dots$ as s, p, d, f, etc. The two-dimensional angular-momentum eigenstates are doubly degenerate, except for the nondegenerate $\ell = 0$ state. As a consequence of this symmetry, the selection rule for transitions between deeply bound levels in such a potential is $\Delta\ell = \pm 1$. However, because this symmetry is broken (usually weakly) by the neighboring strings, the weakly bound states near the top of the potential well can undergo $\Delta\ell = 2$ transitions, although with much lower probability. These considerations are borne out by our many-beam analysis.

The matrix elements, and hence the transition strengths, are computed readily with the many-beam formulation. Since \vec{p} is proportional to \vec{g} , which has the periodicity of the lattice (as do the many-beam representations of the channeling wave functions), we can write the matrix element as

$$\sum_n (c_{\vec{g}_n}^f)^* c_{\vec{g}_n}^i |\vec{g}_n| \quad (16)$$

for the axial case or

$$\sum_n (c_n^f)^* c_n^i (ng) \quad (17)$$

for the planar case. For the axial case the matrix element is usually different along the orthogonal x and y directions, so that it is customary to choose the x-direction to lie along one of the basic transverse reciprocal-lattice vectors, compute $\langle \vec{p}_x \rangle$ and $\langle \vec{p}_y \rangle$, and then define $\langle \vec{p} \rangle^2 \equiv \langle \vec{p}_x \rangle^2 + \langle \vec{p}_y \rangle^2$.

C. Linewidth Calculations

The present calculation of channeling-radiation linewidths takes into account several effects, and the total linewidth is obtained from the quadrature sum of the individual factors.^{10,11} The elements of our linewidth calculations are discussed here in their approximate order of importance.

1. Limited coherence length

Even in a perfect crystal, an energetic charged particle will be scattered by collisions which have small impact parameters with the vibrating atomic nuclei. From the channeling-radiation viewpoint, these collisions have a probability of causing a nonradiative transition of the channeled (radiating) particle either to other bound states or to the unbound continuum; in the latter case, the channeling radiation ceases.

The coherence length of a state is defined as the distance at which the occupation probability of that state decreases to $1/e$ of its initial value. If the transition is from state 2 to state 1, then the total effective coherence length is defined by

$$\frac{1}{\ell} = \frac{1}{\ell_1} + \frac{1}{\ell_2} \quad (18)$$

where ℓ_1 and ℓ_2 are the coherence lengths of the individual eigenstates.

The full-width-at-half-maximum (FWHM) linewidth Γ_{coh} resulting from this mechanism is then

$$\Gamma_{\text{coh}} = \frac{2\gamma^2 \hbar c}{\ell} \quad (19)$$

and the resulting lineshape is Lorentzian.

In order to compute coherence lengths the calculations used here employ a complex potential, the imaginary part of which causes scattering to other states, free or bound. The coherence length of a given state j is given by

$$L_j = - \frac{\hbar \beta c}{2 \langle V_j^i \rangle} \quad (20)$$

where $\langle V_j^i \rangle$ is the expectation value for the energy of the j^{th} state of the imaginary part of the potential. The imaginary parts of the individual Fourier coefficients are written (see Ref. 10) as

$$V_{\vec{g}}^i = - \frac{\hbar^3 \pi}{m^2 c} \frac{S_{\vec{g}}}{V_c} \int_0^\infty f(|\vec{s}|) f(|\vec{s}-\vec{g}|) [e^{-m_{\vec{g}} s} - e^{-m_{\vec{s}} s} - m(\vec{s}-\vec{g})] s \, ds \quad (21)$$

(originally derived by Radi¹²). Here, $V_{\vec{g}}^i$ is the Fourier coefficient of the optical potential for the reciprocal lattice vector \vec{g} and $m_s = u^2 s^2 / 2$ is the Debye-Waller factor. The area of integration is the plane normal to the beam direction.

If Gaussian approximations to the electron scattering factors are used, then the integral can be evaluated in closed form.¹⁰ However, Gaussian parametrizations are not accurate for large values of s , and this fact, although insignificant for eigenvalue calculations, is important here because the high- s Fourier coefficients describe the potential very close to the nucleus (≤ 0.04 Å), where most of the scattering occurs. This is especially important for diamond, because the details of the potential very close to the origin are not as obscured as for other crystal species, owing to its very low thermal-vibration amplitude. In order to take into account the high- s correction to the Gaussian scattering factors, we have performed the integrations numerically. The shift which results from the use of the more

accurate potential (about a 15-to-20% increase in the FWHM linewidth from this source) is significant.

2. Doppler effects

A spread in the linewidth of the radiation from planar-channeled particles arises from the fact that not every particle that radiates is moving directly towards the detector when it does so. This could result from multiple scattering parallel to the channeling planes in the crystal, from nonzero beam divergence, and from other effects as well.

The average scattering angle $\Delta\theta$ resulting from multiple scattering in the crystal can be approximated as¹³

$$\Delta\theta = (14/E_e) \sqrt{Z_0/L} [1 + (1/9) \log_{10}(Z_0/L)] , \quad (22)$$

and

$$\frac{\Delta\omega}{\omega} = (\gamma\Delta\theta)^2 \quad (23)$$

where E_e is the beam energy, Z_0 is the crystal thickness, and L is the radiation length. For the 23- μm diamond crystal of the present experiment, these average multiple-scattering angles range from 2.0 mrad (at 54.5 MeV) to 6.6 mrad (at 16.9 MeV).

This scattering angle applies only for the case of planar channeling, where the electrons are free to scatter in the planar direction while still being channeled between planes. For the case of axial channeling, the channeled particles are constrained in both transverse dimensions, and no broadening from multiple scattering results.

A significant aspect of the line broadening from multiple scattering is that (unlike broadening from coherence-length effects) it is asymmetric, and occurs only on the low-energy side of the calculated (0°) transition energy. This asymmetry results from the fact that the observed transition energy is highest when the channeled particle is moving directly towards the detector when it radiates, and a deflection in any direction will produce the frequency reduction [of $(\gamma\Delta\theta)^2$] noted above. Therefore, we should observe low-energy "tails" for some channeling-radiation transitions, which in fact we do.

Another source of Doppler broadening would be present if the crystal had an appreciable mosaic spread. If the mosaic spread is characterized by an angle θ_m , the electrons would be deflected by a constant θ_m , and a broadening of $\Delta\omega/\omega = (\gamma\theta_m)^2$ would result. The angle θ_m is fixed, so that $\Delta\omega/\omega$ from this mechanism would increase as γ^2 and become dominant at high beam energies. Because this is not observed in our data, we conclude that the diamond crystal that we used has negligible mosaic spread.

Other sources of Doppler broadening might be (a) nonzero crystal and beam size and (b) nonzero detector aperture. In our system, however, these sources are eliminated by two collimators located between the detector and the target which allow the detector to view only a very small portion of the target.

Nonzero beam divergence also is a factor, but because it was only 0.3 to 0.6 mrad for the present experiments, it is negligible in comparison with multiple scattering. Multiple scattering contributes about 5% ($\Delta\omega/\omega$) to the linewidth. Unlike the coherence-length effect, this effect is almost independent of γ , since $\gamma\Delta\theta$ is nearly constant.

3. Bloch-wave broadening

In the many-beam analysis the eigenfunctions are Bloch functions, and the eigenvalues are dependent upon the values of \vec{k}_t or k used in Eqs. (7) or (9). For the lower-lying states, this broadening is completely negligible; however, for states lying near the top of the potential well, this effect can cause considerable broadening, as is illustrated below in the figures of planar potentials.

4. Detector resolution

The resolution of the photon detector has the effect of spreading a monoenergetic line to 2 keV FWHM [for the Ge(Li) detector used for the runs at 16.9 and 54.5 MeV] or to 1 keV FWHM (for the intrinsic Ge detector used for the run at 30.5 MeV). In general, this effect is not as important as the coherence length or Doppler effects.

5. Energy spread of the electron beam

The dependence of the channeling-radiation transition energies on beam energy (γmc^2) is often described as a power law,¹⁹ i.e.,

$$E = E_0 \gamma^\alpha \quad (24)$$

where E_0 and α are constants, with α ranging typically from 1.5 to 2.0 (see below). Taking $\alpha = 1.6$ and noting that the energy spread of the beam for the present experiments was only 0.25%, we observe that a spread in

linewidth of only 0.4% is produced by this mechanism. This is negligible in comparison with the other line-broadening mechanisms discussed above.

6. Finite crystal thickness

Another line-broadening mechanism results from the finite thickness of the crystal. This mechanism is similar but not precisely analogous to coherence-length broadening because when the channeled electrons reach the exit face of the crystal, the occupation probability of any given state does not continue to decrease exponentially as before, but instead drops abruptly to zero. The linewidth from this finite-thickness effect Γ_D is then given by

$$\Gamma_D = 4\pi\gamma^2\hbar c/D \quad (25)$$

where D is the thickness of the crystal.

This mechanism is important when the crystal thickness is comparable to the coherence lengths of the individual eigenstates. For the present case D ($= 23 \mu\text{m}$) is much larger than the coherence lengths, which we calculate to be less than $4 \mu\text{m}$ for almost all of the states involved. Therefore, this mechanism was neglected in our linewidth computations here.

III. EXPERIMENT

A. Experimental Apparatus and Techniques

Although earlier accounts of the experimental apparatus and techniques used for the present measurements have been given in Refs. 11, 14, and 15, a more complete and up-to-date description is presented here.

The Lawrence Livermore National Laboratory Electron-Positron Linear Accelerator is a high-current, five-section, S-band linac, capable of operating between 5 and 170 MeV. When fully loaded (at ~ 70 MeV), its average electron beam current can reach 700 μA . Its maximum (short-) pulse repetition frequency for normal operation is 1440 s^{-1} , which is used for channeling-radiation (or other) experiments for which the counting rates are limited by pileup considerations. Positrons are produced by pair production in a thick, water-cooled, tungsten-rhenium converter positioned several meters downstream from the accelerator, upon which a 120-MeV, 180- μA (average) electron beam is directed and focused (by steering coils and a quadrupole triplet). The positron or electron beam is energy-analyzed with a bending magnet and slit to $\Delta E_e/E_e \approx 0.1 - 0.2\%$ for electrons or to $0.2 - 0.4\%$ for positrons. Its angular divergence is then limited by directing it through a thick copper collimator of diameter 2.4 mm for electrons or 4.9 mm for positrons. The resulting beam current is limited further with the linac gun to a level which results in a counting rate (in the photon detector) which is low enough so that pileup is not significant. The final beam current ranges from a few pA to a few tens of pA, depending upon the species of crystal under study, its diameter, thickness, and orientation, and the beam energy and polarity. The beam-transport system (other than steering coils) up to the

point where the beam enters the experimental cave consists of four dipoles, four quadrupole singlets, and three quadrupole doublets (see Refs. 16 for further details).

Figure 4 shows a schematic diagram of the experimental arrangement used for radiation measurements. After the energy-analyzed and collimated beam of positrons or electrons is transported through a heavy shielding wall into the experimental cave, it is defocused by an asymmetrically split quadrupole triplet to give a low-divergence (nearly parallel) beam incident upon the crystal in its goniometer. After it has passed through the crystal, the charged-particle beam is swept by a magnet into a 5-m deep hole in the floor, through a large paddle-shaped plastic scintillator which serves as a beam current monitor. (The paddle was calibrated against a Faraday cup.) A thick, 4.9-mm diameter tantalum collimator positioned approximately one-third of the way from the crystal to the photon detector limits the angular divergence of the forward photon beam and also prevents the photon spectrometer [a large Ge(Li) or intrinsic-germanium detector] from viewing the crystal holder and other potential sources of background. Another, larger, brass collimator (19 mm in diameter, not shown in Fig. 4) is positioned just upstream of the photon detector, and additional lead shielding surrounds the detector. With this arrangement, background counting rates taken with no crystal in place are negligible.

A critical factor in performing channeling-radiation experiments is the divergence of the incident beam. Since the characteristic angle for the process is $1/\gamma$, an angular resolution at least an order of magnitude smaller is required in order to obtain data of sufficient precision to compare with the results of theoretical calculations; for $\gamma = 100$, for example, a beam divergence larger than 1 mrad is inadequate. Moreover, the critical

angle for channeling is a few mrad for electrons of a few tens of MeV, and varies as $\gamma^{-1/2}$; therefore, in order that a large fraction of the beam be channeled, a beam divergence $\lesssim 1$ mrad is required. The experimental arrangement used for obtaining a very low-divergence beam is shown in Fig. 5; this arrangement is used as well for measurements of the transmission of positrons or electrons through crystals. A CsI scintillator, ruled with grid lines, is placed at the exit window of the vacuum pipe and viewed (through a mirror) with a television camera equipped with an image intensifier for high gain. The television signal is processed by a color quantizer, which assigns a different color to each of ten intervals of intensity. The upper and lower thresholds for each color are independently adjustable. When viewed by a high-quality color-television monitor, this gives a characteristic, multicolored bull's-eye pattern that greatly facilitates beam tuning. The beam is tuned through a removable collimator 9.6 mm in diameter positioned just upstream of the goniometer. With the sweeping magnet off, the beam pipe between this collimator and the CsI scintillator degaussed, and no crystal in the goniometer, the beam is tuned for minimum divergence. This is done by requiring a beam spot on the CsI scintillator that is as nearly as possible the same size as the collimator diameter when nearly 100% of the beam passes through the collimator, as measured with a plastic scintillator paddle positioned just downstream of the CsI scintillator. The actual beam size and shape are measured subsequently with a small plastic scintillator button positioned at the same location. With this scintillator button, the beam is scanned both horizontally and vertically (in the transverse plane), with the CsI scintillator removed. By scanning the beam both with and without the collimator in place, the beam divergence (or convergence) is measured directly. For recent experimental runs, the beam divergence, both for

positrons and for electrons, has been measured to be at the limit of sensitivity of this apparatus ($\lesssim 0.1$ mrad), and hence is no longer a factor in considerations of angular or energy resolution.

With the scintillator button centered on the beam, the tuning collimator and the CsI scintillator removed, a crystal mounted in the goniometer, and the photon collimator (see Fig. 4) inserted along the beam line, the arrangement of Fig. 5 is used to make positron- or electron-transmission measurements. The crystal mapping is achieved most quickly and easily with positron-transmission scans, an example of which is shown in Fig. 6(a). One sees transmission peaks corresponding to planar channeling of the positrons (since the channeling directions are characterized by reduced scattering), from which a map of the crystal, like the one shown in Fig. 7, is constructed. One also can map the crystal, if it is of sufficient size and quality, with electrons, but the transmission dips for electrons (directions of increased scattering) are much smaller in their relative channel-to-random signal ratios than are the corresponding peaks for positrons.

Once the crystal is mapped by planar scans, the locations of the axes can be determined from the intersections of the planes, as can be seen in Fig. 7. When transmission scans are made through an axis, the channel-to-random signal ratios are much larger than for a plane, as shown in Fig. 8. Figure 8(a) shows a positron scan, with its characteristic prominent compensation shoulders (because of the conservation of the number of charged particles) just astride the large channeling peak. Figure 8(b) shows the characteristic "flying-W" pattern for an electron scan; the central peak results from the capture of incident electrons into bound (channeling) states of the deep axial string potential. (The compensation shoulders for electrons are much broader.)

Once a crystal has been mapped, photon spectra can be obtained (with the experimental arrangement shown in Fig. 4). Prior to this, however, it is important to scan the crystal orientation using the photon detector itself, in order to verify that the direction of the crystal plane or axis under study is truly along the beam line, since the positron (or electron) beam might have been deflected slightly by residual magnetic fields during the mapping scans. Figure 6(b) shows the results of such a photon scan for the (110) plane in silicon, where the detected photons between 20 and 130 keV (for incident 54-MeV electrons) are plotted against the crystal tilt angle on a greatly expanded scale. [The width of this peak exceeds the critical angle here because free-to-bound transitions increase the low-energy photon yield in an angular range wider than that over which bound-state channeling occurs; moreover, coherent bremsstrahlung (which are free-to-free transitions) becomes important in the angular region just outside the critical angle.] In favorable cases, the crystal can be mapped entirely by means of photon scans, with no need for transmission scans; but because the data-collection rate for photon spectra is limited by pileup, such a procedure is tedious and time-consuming. Finally, it should be noted that measurements with fine angular resolution require a goniometer capable of small angular steps [the data of Fig. 6(b) were obtained in 0.07-mrad steps].

B. Experimental Parameters

The diamond used for all of the experimental runs reported here is a Type-IIa natural diamond, free from nitrogen-platelet defects. It is 23 μm thick and is cut normal to the $\langle 100 \rangle$ axis.

Three different electron beam energies were used: 54.5, 30.5, and 16.9 MeV. For all energies, the beam was energy-analyzed to less than 0.25%. For the 54.5- and 30.5-MeV runs the angular divergence of the beam incident upon the crystal was ≤ 0.3 mrad FWHM. At 16.9 MeV, the beam divergence was approximately 0.6 mrad FWHM horizontally and 0.4 mrad FWHM vertically (an elliptical beam).

For the 54.5- and 16.9-MeV runs, a Ge(Li) detector was used, with an energy resolution of ~ 2 keV FWHM. The channeling-radiation photons were incident upon this detector after passing through a total of 0.4 mm of aluminum (in the detector and beamline windows). The detector efficiency for this system is constant for photon energies between approximately 30 and 120 keV, and decreases for photons above and below this energy range. The decrease in system efficiency on the low-energy side results mainly from absorption in the aluminum windows.

For the 30.5-MeV run, an intrinsic Ge detector with an energy resolution of ~ 1 keV FWHM was used. The photons incident upon this detector passed through a total of 1.0 mm of beryllium in the detector and beamline windows. This use of beryllium windows greatly enhances the detector-system efficiency in the 30-to-10 keV energy range.

IV. DATA PROCESSING

A. Data Acquisition

Figure 9 shows a block diagram of the data-collection electronics. The heart of the data collection and storage system is a multichannel analyzer (MCA). The detector pulses are amplified by a spectroscopic amplifier and presented to the MCA for pulse-height analysis. The gain of the amplifier is adjusted so that 1024 channels of the MCA span the photon-energy range from zero to ~ 700 keV. A coincidence is demanded between the detector pulse and a gate generated by the accelerator trigger pulse so that a detector pulse is accepted only when the beam is on. The length of an individual data run is preset by gating the electronics "on" until a fixed, predetermined amount of beam flux has passed through the beam monitor (and the crystal).

Current normalization is accomplished by measuring the current from the photomultiplier tube of the beam-monitor (paddle) scintillator in the beam dump with a picoammeter having a voltage output. This output voltage is converted into a series of pulses by a voltage-to-frequency converter. When a preset number of these pulses has been counted by a controller, the controller inhibits the flow of coincidence-gate pulses to the MCA, so that data collection ceases. Using this approach, photon spectra can be normalized properly to one another even when the beam current fluctuates significantly during the experimental runs.

B. Data Reduction

The photon spectra collected by the MCA are calibrated in energy with the use of characteristic spectral lines of several radioisotopes, usually ^{241}Am and ^{137}Cs . The spectra are processed as follows: first, a smoothed background spectrum (obtained with the crystal oriented randomly in a nonchanneling direction) is subtracted, channel by channel, from the data spectrum. This background spectrum usually is obtained for several crystal directions which do not correspond to any axes or planes, and hence it should have no channeling component. A raw data spectrum is shown in Fig. 10, together with a random spectrum below it. The two spectra merge above about 500 keV, where no channeling components (either bound-to-bound or free-to-bound transitions) are expected for this plane and energy; this is a good indication that the current flux has been normalized properly.

After the background spectrum has been subtracted, the remaining spectrum consists of channeling-radiation lines and a "bump" resulting from the free-to-bound transitions. A least-squares curve fit is performed, using Lorentzian lines characterized by independent (and non-interfering) energy, width, and amplitude parameters. (Lorentzians are used because this is the resultant shape when transition linewidths are dominated by coherence-length effects. The use of Gaussian lineshapes produces essentially no shifts in the measured parameters.) In addition, a second-order polynomial is used to simulate the free-to-bound bump to aid the fit. These fits are not unique; different choices for the polynomial sometimes lead to equally good least-squares fits. However, the line energies are always determined quite accurately. The linewidth results also are satisfactory, although they are characterized by uncertainties that are considerably greater than those for

the energies. The amplitude results, however, sometimes vary considerably with the choice of the fitting function. Figure 11 shows the background-subtracted and fitted results for the data spectrum of Fig. 10. All of the spectral results presented in subsequent figures have been corrected for the random-direction background in this manner.

V. RESULTS

A. The (100) Plane

It is of great interest to observe the qualitative changes in the channeling-radiation spectra as the incident electron energy is varied. The (100) plane has the shallowest potential well of the major planes, and at 16.9 MeV only one state ($n = 0$) is bound (the $n = 1$ level is broadened into the continuum), as is shown in Fig. 12(a). No clear transition is observed in the corresponding experimental spectrum, shown in Fig. 12(b), partly because the transition is weak and its expected energy lies well below 20 keV, where the detection system is quite inefficient. At 30.5 MeV, both the $n = 0$ and $n = 1$ states are tightly bound [Fig. 12(c)], and a single strong peak emerges, at 43 keV [Fig. 12(d)]. At 54.5 MeV this $1 \rightarrow 0$ peak has increased in energy to 120 keV [Fig. 12(f)] and has increased in width as well, and a second, weaker peak has emerged at 65 keV, corresponding to the $2 \rightarrow 1$ transition. The width of this latter peak is due almost entirely to the strong Bloch-wave broadening of the $n = 2$ state [Fig. 12(e)].

The measured (100) transition energies (given in Table I) are very well predicted by the many-beam calculations (represented by the vertical lines in Fig. 12 and also given in Table I). For all of the planar calculations, a one-dimensional rms vibrational amplitude of 0.042 Å was used. The electron-scattering factors $f_e(s)$ were obtained from the Gaussian approximations of Doyle and Turner (Ref. 17), using an appropriate correction for the values at large s , where the approximations of Ref. 17 underestimate the scattering factors.

The linewidths, however, are in general underestimated; that is, the

calculations predict considerably narrower linewidths than are actually observed, most markedly for the $1 \rightarrow 0$ spectral line for 54.5-MeV incident electrons. This is discussed in detail in Sec. VI A.

B. The (110) Plane

Because the interplanar spacing between (110) planes is $\sqrt{2}$ times larger than that for (100) planes, the potential for the (110) plane is twice as deep as that for the (100) plane, and has at least three bound states at 16.9 MeV [Fig. 13(a)]. The $1 \rightarrow 0$ transition is observed [Fig. 13(b)] as a strong peak at 23 keV, but the $2 \rightarrow 1$ and $3 \rightarrow 2$ transitions are too low in energy to be observed. Surprisingly, what appears to be a free-to-bound transition from the almost-bound $n = 3$ level to the $n = 0$ state seems to be present at about 42 keV. At 30.5 MeV, four levels are bound [Fig. 13(c)], and all four allowed transitions between them are seen as spectral lines, the $\Delta n = 3$ transition (also see Ref. 9) being at 120 keV [Fig. 13(d)]. At 54.5 MeV, the density of states is higher [Fig. 13(e)], and the transition linewidths are so large that the transitions are starting to blur into one another [Fig. 13(f)] to form a general enhancement. The $4 \rightarrow 1$ $\Delta n = 3$ transition is barely observable at ~ 240 keV.

The measured (110) transition energies also are well predicted by the many-beam calculations (Table I). This indicates that the potentials used here [and also for the (100) case] are probably correct, together with the thermal vibration amplitude (assumed to be isotropic). The linewidths, however, again are markedly underestimated by the calculations, particularly for the low- n transitions. Also, the discrepancies between theory and experiment seem to increase with increasing γ . These discrepancies also are discussed in detail in Sec. VI A.

C. The (111) Plane

As shown in Figs. 14(a) and (c), the potential for the (111) plane in diamond has a double minimum, corresponding to unequally spaced crystal planes. For this case, several transitions combine to form a single strong spectral peak. When the energy of the incident electrons increases from 30.5 to 54.5 MeV, this peak loses much of its strength relative to the free-to-bound bump, and also becomes much broader. At 30.5 MeV [Fig. 14(b)] two $\Delta n = 3$ transitions are visible at approximately 70 and 89 keV, but at 54.5 MeV [Fig. 14(d)] they are virtually indistinguishable.

It is considerably more difficult to assign a calculated peak energy for this plane because the main peak is a composite of six (at 30.5 MeV) or nine (at 54.5 MeV) spectral lines. For the 30.5-MeV case, the strength-weighted mean energy of the six calculated transitions in the peak is 26.8 keV, more than 7% higher than the observed peak at 25.0 ± 0.5 keV. As can be seen in Fig. 15(a), when Lorentzian lines of the calculated widths are fitted to the individual transitions to form a simulated spectrum (the solid curve), it is evident that the calculated linewidths are again much too narrow. According to theory, the large peak should have easily resolvable structure; yet the individual transitions are not observable in the spectrum, except for the $\Delta n = 3$ transitions and the $2 \rightarrow 1$ transition (visible as a small peak at 35 keV). When each transition is arbitrarily and equally broadened just enough (by 4 keV for this case) to obscure the individual lines and produce a single peak, the dashed-curve spectrum in Fig. 15(a) results. This reproduces the observed lineshape quite well (indicating a better linewidth estimate), but the discrepancy in the mean peak energy persists, and is much larger here than any discrepancy for either the (100) or the (110) plane.

At 54.5 MeV, the situation is similar, and the discrepancy is even larger. As can be seen in Fig. 15(b), the individual transitions are not observable, although calculations predict that they should be, showing again that the calculated linewidths are too narrow. When the nine individual transitions again are broadened just enough (by 9 keV for this case) to produce a single peak, the observed lineshape again is reproduced well, but a very large energy shift is evident: the calculated strength-weighted mean energy is 68.4 keV, almost 15% higher than the observed peak at 59.6 ± 0.7 keV. In summary, then, unlike the situation for the other major planes in diamond, the many-beam calculation evidently cannot accurately predict the channeling-radiation transition energies for the (111) plane. This disagreement is discussed in detail in Sec. VI B.

D. The $\langle 100 \rangle$ Axis

The potential for the $\langle 100 \rangle$ axis is much deeper than any of the planar potentials, and has many bound states [approximately twelve even at 16.9 MeV, as shown in Fig. 16(a)]. The number of bound states only can be approximated, since many of the high- n states may be bound or unbound depending upon the value of \vec{k}_t , and Bloch-wave broadening (not shown in Fig. 16) effectively produces a continuum of states near the top of the well for all incident electron energies.

With increasing electron energy, the same trend is observed for the $\langle 100 \rangle$ axis as for the planes. At the lower energies, involving relatively few eigenstates, the transitions are strong and fairly sharp; with increasing electron energy, they increase in number, width, and energy, and decrease in strength relative to the free-to-bound continuum [see Figs. 16(b) and (d)]. At 54.5 MeV, the number of bound states exceeds 30 [Fig. 16(e)], and the measured spectrum [Fig. 16(f)] is essentially featureless, although still considerably enhanced over the continuum.

The calculated $\langle 100 \rangle$ axial transition energies (listed in Table II) agree very well with the measured values. They were obtained with a 13×13 -beam calculation, using a two-dimensional rms vibrational amplitude of 0.060 Å. It is difficult to assign a calculated energy which corresponds with the lowest-energy transitions observed for either 16.9 or 30.5 MeV because there are many transitions which contribute to these peaks. Although the simple strength-weighted average of these transitions yields a reasonable result, it should be remembered that this is only an approximation.

Despite the overall accuracy of these results, there are a few anomalies which merit further discussion. For example, while the energy of the $2p \rightarrow 1s$ transition is very well predicted for 16.9-MeV electrons, it is overestimated

by more than 4% for 30.5-MeV electrons. The reason for this discrepancy is not yet clear. Possibly the detailed shape of the potential very close to the atomic string (where the 1s state is localized) is not well described by our model. The results are better for the lower electron energy (16.9 MeV) because there the 1s state is localized further from the string.

Another curious feature is the fact that although both the $3p \rightarrow 2s$ and the $2s \rightarrow 2p$ transitions are shown by many-beam calculations to be fairly strong [see Fig. 16(d)], they are barely (if at all) discernable in the data. A possible contributing factor be that the 2s state has a very short coherence length because it is localized very close to the atomic string. This would lead to a greatly increased linewidth for any transition for which the 2s level is either the initial or the final state, which in turn would make such transitions difficult to distinguish from the background.

Channeling-radiation spectra for the $\langle 110 \rangle$ axis were obtained as well. However, the $\langle 110 \rangle$ potential well is so deep (~ 130 eV) that there are very many bound states even at 16.9 MeV, and no discrete lines are visible at this or higher energies (only a large general enhancement over the bremsstrahlung background is seen).

VI. DISCUSSION

For channeling-radiation transition energies and strengths, the agreement between the measured and calculated values is quite good for the (100) and (110) planes and for the $\langle 100 \rangle$ axis. However, almost all of the calculations underestimate the observed linewidths. The (111) transition energies also are not predicted accurately (the discrepancy is $\sim 15\%$ for the 54.5-MeV case). These major discrepancies are discussed in more detail in Secs. VI A and B. The subject of the scaling of channeling-radiation energies is discussed in Sec. VI C, and that of level populations in Sec. VI D.

A. Linewidths

The calculated linewidths are underestimated greatly in almost every case. Roughly speaking, their agreement with the measured values is better for transitions between high- n states than for those between low- n states. These high- n states are localized farther from the atoms themselves, and their transition linewidths are dominated by Bloch-wave broadening. For the low- n states, Bloch-wave broadening is negligible, and thermal incoherent scattering is the most important broadening factor. These facts might seem to suggest a deficiency in the calculations of the lifetimes of states resulting from thermal incoherent scattering. However, accurate calculations of the linewidths for silicon and for LiF (Refs. 10 and 18, respectively) have been made within the same theoretical framework. Furthermore, other data with 54-MeV electrons, using a synthetic diamond,² show much narrower linewidths, and are in fair agreement with our calculated values.

A possible explanation for these discrepancies is that the increased linewidths result from electron scattering by crystal defects. Anomalous incoherent scattering would decrease the lifetimes and hence the coherence lengths of the bound states, leading to increased linewidths, as shown by Eq. (18). In a simple model with an average distance (assumed to be isotropic) between defects ℓ_d , the coherence length ℓ_j of a given state j would decrease to ℓ_j' , given by

$$\frac{1}{\ell_j'} = \frac{1}{\ell_j} + \frac{1}{\ell_d} \quad . \quad (26)$$

Assuming that the defects act equally upon all of the eigenstates, one can calculate the effect on the transition linewidths that a given ℓ_d would produce. As can be seen in Table III, the arbitrary assumption that

$\lambda_d = 0.9 \mu\text{m}$ yields "corrected" linewidths which are in much better agreement with the data for the (110) and (100) planes.

The same technique can be applied to the (111) plane. However, there the individual transitions are in general not observable. When a Lorentzian line of the corrected width is fitted to each of the calculated lines and the individual contributions are summed, the resultant calculated spectra [shown below as the dashed curves in Figs. 17(b) and (c), for the 30.5- and 54.5-MeV data, respectively] have linewidths that are much closer to the observed data than the original calculations. The energy shifts persist, but the calculated line shapes are quite similar to those of the data.

In summary, the observed linewidths for all planes are much larger than the calculated linewidths as well as those observed with a synthetic diamond. The assumption of a model incorporating incoherent scattering by defects with an average spacing of $0.9 \mu\text{m}$ yields corrected linewidths which are in reasonable agreement with the observed ones. Since there exists at present no nondestructive method for determining quantitatively the concentration of defects in diamond [or even by transmission electron microscopy (see, e.g., Ref. 19)], the use of channeling radiation as a diagnostic tool might find useful application along these lines.

B. (111) Planar Transition Energies

As shown in Sec. V C, the calculated (111) planar transition energies appear to be considerably higher than the observed ones. This is surprising, since the calculated results for the (100) and (110) planes and for the $\langle 100 \rangle$ axis agree quite well with the data obtained using the same crystal and electron beam. The discrepancy, therefore, must lie in some detail of the calculation (or of the channeling physics) peculiar to the (111) plane.

In the framework of the many-beam formulation, when the electron energy is taken as fixed, the following factors have a direct influence upon the apparent position of a peak which is composed of several transitions, as is the case for the (111) plane: (a) the thermal-vibration amplitude; (b) the individual level populations; and (c) the shape and depth of the potential function.

Of these factors, a significant change in (a) is unlikely because the (100) and (110) results using the same thermal-vibration amplitude fit the data quite well. Implicit in the derivation of the Debye-Waller factor is the Einstein approximation, which assumes the presence of independently, isotropically vibrating atoms. In the tight diamond lattice (at room temperature) this might not be strictly the case, but, in our judgment, it is not an assumption that can be abandoned easily.

As for factor (b), all of the calculated spectra contain the implicit assumption that all of the eigenstates are populated equally. If this were not the case, then the strengths of each of the individual transitions would need to be multiplied by the (normalized) fractional population of the initial state of the transition. If, for example, at 30.5 MeV the population of the $n = 3$ level were only half that of its neighbors, the apparent strength of the

3 \rightarrow 2 transition at 30 keV would be reduced, and the calculated location of the composite peak would be shifted downward, closer to the location of the observed peak.

However, there are at least two reasons to doubt this hypothesis. First, multiple scattering tends to equalize the populations of all levels quickly, within a few microns of the entry face of the crystal.¹⁸ If this were not the case, anomalous strength distributions should be present for some of the other planes as well, and this is not true. Second, at 30.5 MeV, the 3 \rightarrow 0 and 4 \rightarrow 1 transitions are visible, and they, too, are shifted in energy. Since an unequal population distribution would affect the strengths but not the energies, it would have no effect upon the location of an isolated peak. Therefore, an anomalous population distribution appears to be an unlikely mechanism to explain the energy shifts.

Turning, therefore, to factor (c), we know that the shape and depth of the potential function is the most important factor governing the energy eigenvalues and hence the transition energies. The potentials used in our calculations are based upon Hartree-Fock calculations of isolated (spherical) atoms. These calculations are incorrect for this case because the electron distributions in the crystal are nonspherical.

Evidence for the effect of anisotropy of the electron distribution in diamond in $\langle 110 \rangle$ axial channeling-radiation spectra has been presented in Ref. 1. Just as there is an alternation of string spacings perpendicular to the $\langle 110 \rangle$ axial direction, so is there an analogous alternation of planar spacings perpendicular to the (111) planar direction. Therefore, one would expect any modification of the potential by redistribution of the electrons to be discerned most easily for this plane.

The measurement of the electron distribution in the covalent bond of diamond has been the object of considerable research effort.^{20,21} The most easily quantifiable results are those of x-ray diffraction experiments (Ref. 20; see also Ref. 21) where the experimentally determined intensities of several x-ray Bragg reflections are found to be considerably different from those which are predicted from standard theory, which assumes a spherically symmetric charge distribution. These studies all conclude that there is an enhanced electron density along the bond, and that the charge density in the middle of the bond is about 1.7-1.8 electrons/Å³. We should, therefore, be able to use the results of some of these studies to determine an experimentally based potential for the (111) plane.

The intensity of x-ray reflections is proportional to the square of the kinematic x-ray scattering factor $f_x(s)$, where $s = ng/4\pi$. This in turn is dependent upon the charge distribution $\rho(r)$ within the atom [just as $f_e(s)$ is dependent upon the atomic potential, as shown in Eq. (10)]¹⁷:

$$f_x(s) = \frac{8\pi^2 me}{h^2} \int_0^\infty r^2 \rho(r) \frac{\sin(4\pi sr)}{4\pi sr} dr \quad (27)$$

The x-ray scattering factor can be related to the electron scattering factor by

$$f_e(s) = \frac{2}{a_0} \frac{1}{(4\pi s)^2} [Z - f_x(s)] \quad (28)$$

where a_0 is the Bohr radius, \hbar^2/me^2 . Thus any change in the x-ray scattering factor $\Delta f_x(s)$ can be related to a corresponding change in the electron scattering factor $\Delta f_e(s)$ by

$$\Delta f_e(s) = - \frac{2}{a_0} \frac{1}{(4\pi s)^2} \Delta f_x(s). \quad (29)$$

These changed electron scattering factors then can be used to determine new Fourier coefficients of the planar potential [by Eq. (12)] which in turn are used in the standard many-beam calculation.

The experimental data of Ref. 20 show considerable shifts in $f_x(s)$ for the first two reflections along the (111) line. They indicate that $\Delta f_x = 0.26$ for the (111) reflection and $\Delta f_x = 0.15$ for the (222) reflection. It should be noted that a measured $f_x(s)$ is influenced by the appropriate structure factor (see Ref. 21 for details) and already includes thermal-vibration effects.

These changes in the scattering factors lead to changes in the Fourier coefficients v_1 and v_2 . The resultant potential, which we shall refer to as the (111A) potential, together with its eigenvalues for 30.5-MeV electrons, is shown in Fig. 17(a) as a light solid curve, along with the old potential shown as a dashed curve. The eigenvalues for 54.5-MeV electrons are not shown because of the many bound states involved. As can be seen, the (111A) potential is considerably shallower in the region of the planes themselves. This decreased depth can be understood qualitatively by considering the enhanced density of bonds between the two closely spaced planes of atoms. If the electron concentration in the bonds is increased as expected, then the extra negative charge will raise the potential for incident electrons, which is indeed what is observed.

The calculated spectra illustrated by the dashed curves in Figs. 17(b) and (c) are obtained by fitting the defect-corrected linewidths calculated by the methods outlined in Sec. VI A to the transition energies and strengths computed using the "standard" potential [Figs. 14(a) and (c)]. The calculated spectra shown by the light solid curves in Figs. 17(b) and (c) are obtained by the same method, using the defect-corrected linewidths applied to the

transition energies and strengths computed using the (111A) potential. It can easily be seen that the results of the computations using the (111A) potential are in much better agreement with the data than are those using the standard potential, both for the peak energies and for the linewidths.

For 30.5-MeV electrons, both the energy and width of the main peak are predicted very well, and the energies of the two $\Delta n = 3$ transitions also are in better agreement: 73.6 keV calculated vs. 72 ± 1 keV observed for the $3 \rightarrow 0$ transition (a 2% discrepancy), and 92 keV calculated vs. 89 ± 1.5 keV observed for the $4 \rightarrow 1$ transition (a 3% discrepancy). Using the standard calculation, the energies for these transitions disagree with the data by 6% and 10%, respectively.

However, the $2 \rightarrow 1$ transition appears to disagree by 5% (36.3 keV calculated vs. 34.5 ± 1 keV observed). It also is not clear why more structure is not observed in the data, as would be suggested by either of the synthetic spectra.

For 54.5-MeV electrons, considerable improvement again is evident; both the width and the shape of the main peak are predicted very well. The peak energy, however, still is overestimated by 5%, (62.8 keV calculated vs. 59.8 ± 1 keV observed), which is nevertheless a great improvement over the previous discrepancy of almost 15%. Although it is very difficult to extract from the data, a $\Delta n = 3$ transition appears to be present at about 154 ± 5 keV. This compares with a calculated value of 162 keV for the $3 \rightarrow 0$ transition, a discrepancy of only 5%, compared with one of 9% for the calculation based upon the old potential.

This improvement in the calculated results indicates that the corrected, experimentally based (111A) potential is a better representation of the true (111) potential than is the standard potential and thus shows that the

electrons are redistributed along the bond in a manner which probably is quite similar to that suggested in Refs. 20 and 21. The authors of Ref. 1 have analyzed the radiation from 4-MeV electrons channeled along the $\langle 110 \rangle$ axis of diamond to compute a bond-charge redistribution which also is very similar to that of Ref. 20.

We now explore the effects of further modifying the (111) potential. A hypothetical potential in coordinate space can be postulated, and Fourier transformed numerically. Then the Fourier coefficients v_n can be extracted, and the new energy eigenvalues and eigenvectors can be computed as before, via the many-beam formulation. The accuracy of this technique can readily be checked by using the unchanged Fourier coefficients v_n to obtain a standard potential in coordinate space, Fourier-transforming the coordinate-space potential numerically, and using the newly extracted Fourier coefficients v_n' to calculate new energy eigenvalues which then can be compared with the previous values. The results are accurate easily to within 1%, which is less than the other sources of experimental uncertainty.

We have used this technique to modify the standard (111) potential, and have found a new potential, derived on the basis of providing a best fit to the 30.5-MeV data. This new potential V' is related to the standard (Hartree-Fock) potential V by the empirical relation

$$V'(x) = V(x) + 1.7 \exp(-x^2/0.1) - 0.75 \exp[-(|x| - 0.6)^2/0.1]. \quad (30)$$

This empirical potential, which we shall refer to as the (111B) potential, together with its (30.5-MeV) eigenvalues, is shown in Fig. 18(a) as a heavy solid curve, along with the standard potential, shown as a dashed curve, and the the (111A) potential, shown as a light solid curve. It can be seen that the (111B) potential involves considerably less change from the standard (111)

potential than does the (111A) potential. Interestingly, it dips below the standard potential in the region around $x = \pm 0.6 \text{ \AA}$. This slight dip turns out to be rather important in determining the shape of the calculated spectra for this potential because it alters the shape of the potential in the region where the eigenstates that take part in the bulk of the transitions in the major spectral peak are localized.

These calculated spectra [which were obtained using the same methods as were used for the calculated spectra of Figs. 17(b) and (c)] are shown as the heavy solid curves in Figs. 18(b) and (c) (for 30.5- and 54.5-MeV electrons, respectively). For comparison purposes, the calculated spectra obtained from the use of the (111A) potential are shown as the light solid curves. It is seen that the (111B) potential is slightly better than the (111A) potential for 30.5-MeV electrons, particularly with respect to the width of the main peak and the energy of the $3 \rightarrow 0$ transition. Moreover, the prediction of the (111B) potential for the energy of the main peak of the 54.5-MeV spectrum results in a discrepancy of less than 2%, considerably smaller than the 5% discrepancy for the (111A) potential. This is very gratifying because the (111B) potential was deduced solely from a fit to the 30.5-MeV data.

It is not certain whether the (111B) potential is consistent with the other data pertinent to the electron distribution along the (111) bond. However, the higher-order x-ray scattering factors are weak and difficult to determine from diffraction measurements; therefore, this channeling-radiation technique may provide us with a valuable means of investigating these higher-order terms. In any case, it is clear that either of the two shallower potentials discussed here would produce predictions that are in better agreement with the positron channeling-radiation data of Ref. 3. Finally, it is encouraging that these potentials work well for electrons at two well

separated energies; but certainly more theoretical and experimental results (especially at lower energies, where the $\Delta n = 1$ transitions should be individually resolvable) would be very illuminating.

C. Energy Scaling

The electron-beam energies of our experiments ranged from 16.9 to 54.5 MeV, and other data for diamond extend this range both to higher [80.2 and 110.2 MeV (Ref. 22)] and to lower [4.0 MeV (Ref. 1)] energies. Therefore, we can observe how channeling-radiation energies scale over a very wide range of incident electron-beam energies ($8.8 \leq \gamma \leq 217$).

When a one-dimensional potential is described by a power law, i.e., $V(x) = ax^m$, where x is measured from the midpoint between the planes in the direction normal to them, then the eigenvalues in the rest frame will scale as $\gamma^{2/(m+2)}$ (Ref. 18). The transition energies will scale as $\hbar\omega_r = a\gamma^\alpha$, where $\alpha = 2/(m+2)$. Multiplying these rest-frame energies by 2γ to obtain the observed photon energies in the laboratory frame, we should observe photon energies scaling as $\hbar\omega_\ell = 2E_0\gamma^{[1 + 2/(m + 2)]}$, where E_0 is a constant.¹⁸

Qualitatively, most electron planar potentials appear to be "V-shaped" around the origin (at the plane), except very close to it, and flatten out gradually as x approaches $d_p/2$, where d_p is the interplanar spacing. Thus $m \approx 1$ for eigenstates which are localized relatively close to the planes, and $m \approx 0$ for eigenstates which are localized farther away from them.

Figure 19 shows how the eigenstates are localized for a typical plane at the three energies of our experiment. As expected, the low- n eigenstates are localized close to the planes and the higher- n ones farther away. For the plane shown, the highest eigenstate is not even localized to a single plane. Therefore, we expect the $1 \rightarrow 0$ transition to scale approximately as $\hbar\omega_\ell \propto \gamma^{5/3}$, and high- n transitions such as the $3 \rightarrow 2$ or $4 \rightarrow 3$ transitions to scale approximately as $\hbar\omega_\ell \propto \gamma^2$.

Assuming that the transition energies scale as $\hbar\omega_\ell = b\gamma^\alpha$, we obtain

values for α by taking the photon energies at two different values for γ , from which

$$\alpha = \ln \left\{ \frac{\hbar\omega_1}{\hbar\omega_2} \right\} / \ln \left\{ \frac{\gamma_1}{\gamma_2} \right\} . \quad (31)$$

Figure 20 shows the plot of $\log_{10}(\hbar\omega)$ vs. $\log_{10}(\gamma)$ for all of the available planar transitions.

We see that, as expected, α is higher for the high- n transitions than for the low- n transitions. For example, for the $1 \rightarrow 0$ transition for the (110) plane, the average value for α is 1.67; for the $2 \rightarrow 1$ transition it is 1.83; and for the $3 \rightarrow 2$ transition it is 1.92. From the simple theory one would expect α to increase from 5/3 to 2 with increasing n , and indeed this is the case.

All of the numerical results of this analysis are listed in Table IV. We observe that for any transition other than the $1 \rightarrow 0$ transition α tends to decrease with increasing γ . This is entirely consistent with the above model, for as the beam energy (γ) increases, the energy of an eigenstate decreases (it moves down in the potential well) as its wave function becomes increasingly localized near the atomic plane. Thus, transitions which are effectively high- n transitions at a low beam energy eventually become low- n transitions at higher beam energies, with a concomitant decrease in α . This effect can be seen clearly here for the case of the (110) $2 \rightarrow 1$ and $3 \rightarrow 2$ transitions.

D. Bound-State versus Free-State Populations

A decrease of channeling-radiation line strengths [bound-to-bound (B-B) transitions] relative to the background bump [which consists of both free-to-bound (F-B) and free-to-free (F-F) transitions] as the incident electron-beam energy increases is a common feature for all of the planes and axes in the energy range of our experiment. (This is also true for the data of Ref. 22.) This is puzzling because we know that the strength of a spectral line is proportional to its energy (see Sec. II B), which always increases with electron-beam energy (as is discussed in Sec. VI C). Therefore, the overall intensity of the F-B and F-F components must increase with beam energy at some rate faster than that of the B-B component (the "random" bremsstrahlung spectrum, which increases linearly with incident beam energy, has already been subtracted from the data).

A possible reason for this phenomenon is that the strengths of the individual F-B and F-F transitions increase with beam energy faster than those of the B-B transitions. However, an extension of our many-beam calculation to the first several free states shows that this increase does not occur. Therefore, it must be the case that the overall population of the free states increases significantly relative to that of the bound states as the beam energy increases.

This occurs for two reasons: the first is that as the beam energy increases, the critical angle for channeling becomes smaller, and fewer electrons are initially captured into bound states. A calculation shows, if we assume a constant beam divergence of 0.3 mrad, that the percentage of electrons captured initially into the bound states of (110) diamond varies from about 99% at 16.9 MeV to about 70% at 54.5 MeV. However, it is important

to remember that these values are for the initial populations only, and that the populations are redistributed by incoherent scattering mechanisms (discussed in Sec. II C) well before the electrons have traversed a significant portion of the crystal. In our calculations of relative line strengths, we always assume the initial populations of the bound states to be equal, and this assumption always has yielded good results. This population redistribution by incoherent scattering is the most important reason for the increase of the free-state population, because as the electron-beam energy increases, the channeling wave functions draw closer to the planes or strings, and incoherent scattering to other states is strongly enhanced. [Figure 19 illustrates graphically this drawing together of the (squares of the) wave functions.] Some of these states may be bound; however, the total number of available unbound states is much greater than the number of bound states, so that the net effect is a depopulation of the bound states with respect to the free states. As an example of this effect, the coherence length of the $n = 1$ state of (110) diamond at 16.9 MeV is 4.0 μm , whereas the coherence length of the same state at 54.5 MeV is only 2.2 μm .

VII. THE APPLICABILITY OF CHANNELING RADIATION AS A PHOTON SOURCE

The ratios of the intensities of channeling radiation and bremsstrahlung for some of the diamond axes and planes at 16.9 MeV and 30.5 MeV are among the highest that we have observed for any crystal or energy. It is therefore of great interest to estimate the amount of channeling radiation obtainable from such a crystal in order to investigate its applicability as a photon source. To do this, the amount of bremsstrahlung produced in the crystal for a given electron flux is calculated, and an estimate of the channeling-radiation intensity is made using the observed intensity ratios.

Assuming complete screening of the nuclear charge (valid for the frequency interval of those photons for which $\hbar\omega \ll E_e$, where E_e is the electron-beam energy), one obtains for the doubly differential radiation cross section for relativistic bremsstrahlung²³:

$$\frac{\# \text{ photons}}{\text{electron-cm}} = 1.47 \times 10^{-27} N_V \frac{\gamma^2 Z^2}{\beta^2} \ln \left\{ \frac{233}{Z^{1/3}} \right\} \left\{ \frac{1 + \gamma^4 \theta^4}{(1 + \gamma^2 \theta^2)^4} \right\} \frac{d\omega}{\omega} d\Omega \quad (32)$$

where N_V is the number of atoms per cm^3 , Z is the atomic number, $\beta = [(\gamma^2 - 1)/\gamma^2]^{1/2} = v/c$, $\hbar\omega$ is the photon energy, Ω is the solid angle, and θ is the angle between the electron beam line and the observation point.

The maximum allowable value for θ for a bandwidth $\Delta\omega/\omega = 10\%$ is computed from the equation for the relativistic Doppler shift

$$\frac{\Delta\omega}{\omega} = \frac{\beta(1 - \cos\theta)}{1 - \beta\cos\theta} \quad (33)$$

from which one obtains $\theta = 5.5 \text{ mrad}$ for 30.5-MeV electrons. Integrating the θ -dependent part of Eq. (32) numerically and solving for a beam energy of 30.5 MeV, one obtains an intensity of 1.3×10^{-3} photons/electron-cm in a

10% bandwidth, out to an angle of 5.5 mrad. Our crystal is 23 μm thick, so we can expect 3×10^{-6} bremsstrahlung photons/electron in this frequency range.

A reasonable estimate for the maximum average current readily attainable from the LLNL linac is $\sim 100 \mu\text{A}$ in a 5-mm-diameter beam. For this current, we obtain $\sim 2 \times 10^9$ bremsstrahlung photons/second.

The highest ratio of channeling radiation to bremsstrahlung that we have observed is for the 58-keV line of the $\langle 100 \rangle$ axial spectrum for 16.9-MeV electrons, which is 9.5:1. However, this is not an isolated line, but is surrounded by other transitions as well as by a large free-to-bound component. By contrast, the ratio for the $1 \rightarrow 0$ transition in the (100) planar spectrum for 30.5-MeV electrons is 7.1:1 (at 43 keV) and the ratio for the $1 \rightarrow 0$ transition in the (110) planar spectrum for 16.9-MeV electrons is 6.3:1 (at 23 keV), and these spectral lines are well isolated. These latter, therefore, should be more suitable for use as a monochromatic photon source, and are linearly polarized as well.

Thus, for 16.9-MeV electrons channeled along the (110) plane, we compute 1.15×10^{10} photons/second in a 10% bandwidth at 23 keV. For 30.5-MeV electrons channeled along the (100) plane, we compute 1.3×10^{10} photons/second in a 10% bandwidth at 43 keV.

It also is necessary to calculate the expected crystal damage in order to ascertain whether it is feasible to run at such a high beam current. Crystal damage falls into two categories: radiation damage from the high-energy electron beam and heating from collisional energy loss of the electrons as they pass through the crystal. Both of these depend upon beam energy and current, which we will take as $100 \mu\text{A}$ in a 5-mm-diameter beam at 30.5 MeV (the figures for 16.9 MeV will be more favorable).

The high-energy electron beam passing through the crystal will damage the crystal by knocking atoms out of their lattice sites. The fraction of electrons producing such knock-ons is

$$\frac{\Delta N}{N_e} = N_v \sigma \Delta Z \quad (34)$$

where N_v is the number of atoms per unit volume, σ is the cascade displacement cross section, ΔZ is the sample thickness, ΔN is the number of knock-ons, and N_e is the total number of electrons. Therefore the fraction of displaced atoms is

$$\frac{\Delta N}{N_{at}} = \frac{\Delta N}{N_v A \Delta Z} = \frac{N_e \sigma}{A} \quad (35)$$

where N_{at} is the total number of atoms being irradiated and A is the area of the beam.

Assuming a mean displacement energy of 24 eV to remove a diamond atom from its lattice site, we obtain $\sigma \approx 72 \text{ b.}^{24}$ For the previously specified beam parameters, we then can expect that $\Delta N/N_{at} \approx 8.2 \times 10^{-4}$ for one hour; i.e., about one atom in 1200 is displaced in one hour of operation. This is not a large fraction, and it would seem that knock-ons would not limit operation, at least for many hours.

The collisional energy deposited by the electrons as they pass through the crystal can be written as²⁵

$$E_{col} = 2\rho C(mc)^2 \ln \left\{ \frac{\pi^2 (mc^2)^2}{[(1 - \beta^2)^{3/2}] I^2(Z)} \right\} \quad (36)$$

where $C = 0.15 Z/A$, ρ is the density in g/cm^3 , and I is the ionization potential [about 60 eV for $Z = 6$ (carbon)]. Allowing for the density effect,²⁵ this leads to an energy dissipation of approximately 8.8 MeV/cm

per electron passing through the crystal. This means that a 23- μm diamond crystal will have to dissipate ~ 2.0 W. Assuming only radiative cooling, this implies that the crystal will heat up to approximately 800°C . The crystal still will remain intact at this temperature, but the rms vibrational amplitude of the atoms will be increased. The (one-dimensional) thermal vibration amplitude u_1 is related to the crystal temperature T and the Debye temperature θ by:

$$u_1 = 12.1 \left\{ \left[\phi\left(\frac{\theta}{T}\right) \frac{T}{\theta} + 0.25 \right] / M\theta \right\}^{1/2} \quad (37)$$

where M is the atomic weight of the crystal atoms in amu and $\phi(x)$ is the Debye function

$$\phi(x) = \frac{1}{x} \int_0^x \frac{s}{(e^s - 1)} ds \quad (38)$$

Diamond has a very high Debye temperature (~ 2000 K), so that increasing the crystal temperature from room temperature to 810°C increases the one-dimensional thermal-vibration amplitude from 0.042 Å only to 0.060 Å. The effect of this increase is to make the potential somewhat shallower in the center, so that the transition energies are reduced slightly. However, 800°C is approximately the temperature needed to anneal out light radiation damage from diamond crystals, so that the above computation of the number of knock-on defects is an overestimate, and the crystal might in fact be self-annealing.

The calculated spectrum for 30.5-MeV electrons channeled along the (100) plane in diamond at 810°C (neglecting random and free-to-bound components) is shown, together with the spectrum for 25°C , in Fig. 21. It can be seen that the calculated spectrum for the higher temperature shows slightly increased linewidths and decreased intensity. Based upon these results, we compute (as

before) approximately 1.1×10^{10} photons/second in a 10% bandwidth at 40.6 keV.

In comparison, the Stanford Synchrotron Radiation Laboratory 8-pole wiggler, operated at 18 kG with a 3-GeV electron beam will produce approximately 5×10^{12} photons/second-mA-mrad at 40 keV. This is broadband radiation, however, and therefore a monochromator usually has to be used. Thus, channeling radiation is not as bright (at this relatively low energy) as a high-energy synchrotron-radiation source at high current. However, the intensity of synchrotron radiation drops precipitously with photon energy while that of channeling radiation increases, so that for photon energies of the order of 100 keV or higher channeling radiation becomes the more intense source. In any case, even at low energies, it can be seen that channeling radiation from diamond can serve well as an intense, narrowband, polarized source of x rays which can be utilized at many existing smaller accelerators.

VIII. SUMMARY AND CONCLUSIONS

A series of electron channeling-radiation experiments has been performed using a type-IIa natural diamond as target. Spectra were collected for electron beams from the Lawrence Livermore National Laboratory Electron-Positron Linear Accelerator of energies 16.9, 30.5, and 54.5 MeV incident along the (100) and (110) planes and the $\langle 100 \rangle$ axis, and of energies 30.5 and 54.5 MeV along the (111) plane. Detailed expositions of both the experimental techniques and the theoretical calculations used by our group have been given (Figs. 1-11).

The channeling-radiation spectra contain sharp and prominent structure. For the (100) and (110) planes and for the $\langle 100 \rangle$ axis, one- and two-dimensional (respectively) many-beam calculations yield transition energies in generally good agreement with the locations of the spectral peaks (Tables I and II, Figs. 12, 13, and 16). This good agreement indicates that the standard (Hartree-Fock) potential and thermal-vibration amplitudes used as input for these calculations are nearly correct, and that the theory is basically sound. However, calculations using the standard potential overestimate significantly the energy of the main peak of the (111) spectra, which is a composite of several individual transitions (Fig. 14).

The linewidths observed for the spectra collected using 54.5-MeV electrons are approximately twice as large as those observed by the authors of Ref. 2 who used an unusually perfect region of a synthetic diamond. They also are considerably broader at all energies than predicted by calculations. Since accurate linewidth calculations for Si and LiF were made using the same theory (Refs. 10 and 18), it is concluded that the above discrepancies result from the properties of the particular diamond crystal used for these experiments.

Calculations using a simple model which postulates increased incoherent scattering by crystal defects of a constant average spacing yield increased linewidths, in reasonable agreement with the observed data (Table III, Fig. 15). An average defect spacing of 0.9 μm was deduced using this method. This technique may provide a quantitative assessment of the defect density in diamond crystals. When defect-corrected linewidths are fitted to the calculated transition energies for the (111) plane, the major discrepancies in the location of the main spectral peak can be quantified (7% for 30.5-MeV electrons and 15% for 54.5-MeV electrons).

Using a potential based upon x-ray-diffraction data for diamond [the (111A) potential] yields calculated results which are in much better agreement with the data (Fig. 17). The energy of the main (composite) spectral peak is predicted almost precisely for the 30.5-MeV spectrum and within 5% for the 54.5-MeV spectrum. Further, an empirical potential [the (111B) potential] was derived on the basis of providing a best fit to the 30.5-MeV data. The calculated results for the (111B) potential are slightly better than for the (111A) potential at 30.5 MeV (especially for the location of the $\Delta n = 3$ transitions), and moreover, the position of the spectral peak in the 54.5-MeV data is much better predicted [2% error for the (111B) potential vs. 5% for (111A) potential] as well (Fig. 18). In this way, channeling-radiation data may provide a means for quantifying higher-order x-ray scattering factors, which cannot be done with x-ray-diffraction data alone.

The transition energies have been shown to scale as a power-law function of the electron-beam energy. Those transitions involving states which are localized close to atomic planes scale as $\hbar\omega \propto \gamma^{5/3}$, while the scaling of transitions involving states that are localized closer to the midplane regions approaches $\hbar\omega \propto \gamma^2$ (Table IV, Figs. 19 and 20). This is consistent with a qualitative

description of the planar potential as a power law; i.e., $V(x) = ax^m$, with $m \approx 1$ near the plane and $m \approx 0$ at midplane.

Random-subtracted spectra obtained from the same plane at different beam energies show that the strengths of the bound-to-bound transitions relative to the background bump (consisting of free-to-bound and free-to-free transitions) consistently decrease as the incident beam energy increases (see, e.g., Figs. 12-14 and 16). Since many-beam calculations do not indicate an increase in the strengths of the free-to-bound transitions relative to the bound-to-bound transitions with increasing beam energy, it is concluded that the populations of the free states increase with respect to the bound-state populations as the incident electron-beam energy increases. This occurs for two reasons: first, it is likely that somewhat fewer electrons are trapped into bound states at higher beam energies because of the decrease in the critical angle; and second, incoherent scattering is strongly enhanced at higher energies, leading to a more rapid depopulation of the bound states, which results in a lower average population in these states.

Thus, we have seen that the channeling-radiation spectra from diamond presented here contain a wealth of information and shed light on a variety of channeling phenomena and crystal properties. Finally, we have demonstrated quantitatively the potential usefulness of channeling radiation as an intense source of narrowband, sharply focused, polarized x-rays.

ACKNOWLEDGMENTS

The authors are very grateful to Prof. J.P.F. Sellschop for providing the diamond. We also thank Dr. Z.-H. Bian for help in computer programming and J. Pressessky for useful discussions.

This work was performed at Lawrence Livermore National Laboratory under the auspices of the U.S. Department of Energy under Contract No. W-7405-ENG-48, and was supported as well by the U.S. Air Force Office of Scientific Research under Grant No. AFOSR-81-0209, by the U.S. Joint Services Electronics Program under Grant No. DAAG-29-81-K-0057, and by the National Science Foundation under Grant No. ECS-18139. Two of us (S.D. and R.W.F.) acknowledge the support of the Office of Basic Energy Sciences, U.S. Department of Energy, under Contract No. W-7405-ENG-26 with Union Carbide Corporation; one of us (R.W.F.) also acknowledges the support of the Council for Scientific and Industrial Research of South Africa.

REFERENCES

1. J. U. Andersen, S. Datz, E. Laegsgaard, J. P. F. Sellschop, and A. H. Sørensen, Phys. Rev. Lett. 49, 215 (1982).
2. M. Gouanère, D. Sillou, M. Spighele, N. Cue, M. J. Gaillard, R. G. Kirsch, J.-C. Poizat, J. Remillieux, B. L. Berman, P. Catillon, L. Roussel, and G. M. Temmer, Nucl. Instrum. Methods 194, 225 (1982).
3. S. Datz, R. W. Fearick, H. Park, R. H. Pantell, R. L. Swent, J. O. Kephart, R. K. Klein, and B. L. Berman, Phys. Lett. 96A, 314 (1983).
4. H. Park, R. H. Pantell, R. L. Swent, J. O. Kephart, B. L. Berman, S. Datz, and R. W. Fearick, J. Appl. Phys. 55, 358 (1984).
5. V. B. Ganenko, I. I. Miroshnichenko, E. V. Pegushin, V. M. Sanin, and S. V. Shalatskij, Radiat. Effects 62, 167 (1982).
6. I. I. Miroshnichenko, J. J. Murray, R. O. Avakyan, and T. Kh. Figut, Pisma Zh. Eksp. Teor. Fiz, 29, 786 (1979) [JETP Lett. 29, 722 (1979)].
7. J. U. Andersen, S. K. Andersen, and W. M. Augustyniak, Kgl. Dan. Vidensk. Selsk. Mat.-Fys. Medd. 39, No. 10 (1977).
8. L. I. Schiff, Quantum Mechanics (McGraw-Hill, New York, 1968), p. 414.
9. B. L. Berman, S. D. Bloom, S. Datz, M. J. Alguard, R. L. Swent, and R. H. Pantell, Phys. Lett. 82A, 459 (1981).
10. R. L. Swent, Ph.D. thesis, Stanford University (1982).
11. R. H. Pantell, H. Park, R. L. Swent, J. O. Kephart, R. K. Klein, S. Datz, and B. L. Berman, IEEE Trans. Nucl. Sci. NS-30, 3150 (1983).
12. G. Radi, Acta. Cryst. A26, 41 (1970).
13. M. J. Alguard, R. L. Swent, R. H. Pantell, B. L. Berman, S. D. Bloom, and S. Datz, Phys. Rev. Lett. 42, 1148 (1979).

14. M. J. Alguard, R. L. Swent, R. H. Pantell, B. L. Berman, S. D. Bloom, and S. Datz, IEEE Trans. Nuc. Sci. NS-26, 3865 (1979).
15. B. L. Berman and S. D. Bloom, Energy Tech. Rev. 81-1, 1 (1981).
16. B. L. Berman and S. C. Fultz, University of California Lawrence Livermore Laboratory Report No. UCRL-75383 (1974) and Rev. Mod. Phys. 47, 713 (1975).
17. P. A. Doyle and P. S. Turner, Acta Cryst. A24, 474 (1968).
18. R. L. Swent, R. H. Pantell, H. Park, J. O. Kephart, R. K. Klein, S. Datz, R. W. Fearick, and B. L. Berman, Phys. Rev. B 29, 52 (1984).
19. T. Evans, Contemp. Phys. 17, 45 (1976).
20. S. Göttlicher and E. Wölfel, Z. Electrochem. 63, 891 (1959).
21. B. Dawson, Proc. Roy. Soc. A298, 264 (1967).
22. M. Gouanère, D. Sillou, M. Spighel, N. Cue, M. J. Gaillard, R. Kirsch, J.-C. Poizat, J. Remillieux, B. L. Berman, P. Catillon, L. Roussel, and G. Temmer, Proc. Tenth Int. Conf. on Atomic Collisions in Solids (Bad Iburg, 1983).
23. J. D. Jackson, Classical Electrodynamics (Wiley, New York, 1975) p. 713.
24. O. S. Oen, Oak Ridge National Laboratory Report No. ORNL-4897 (1973).
25. B. Rossi, High-Energy Particles (Prentice-Hall, New York, 1952), p. 27.

Table I. Planar transition energies and linewidths.

Plane and Beam energy	Transition	Observed energy (keV)	Calculated energy (keV)	Observed linewidth (keV)	Calculated linewidth (keV)
(100)					
16.9 MeV	1 \rightarrow 0	not observed	14.4	not observed	5.65
30.5 MeV	1 \rightarrow 0	43.0 \pm 0.3	43.7	5.9 \pm 0.3	5.5
54.5 MeV	1 \rightarrow 0	119.8 \pm 0.7	120.6	18.7 \pm 0.7	7.3
	2 \rightarrow 1	64.7 \pm 1.5	63.2	23.8 \pm 3.0	20.3
(110)					
16.9 MeV	1 \rightarrow 0	23.3 \pm 0.4	22.9	3.3 \pm 0.4	2.3
	2 \rightarrow 1	not observed	11.6	not observed	3.1
	3 \rightarrow 0	41.6 \pm 0.7	42.8	13.8 \pm 1.5	8.1
30.5 MeV	1 \rightarrow 0	60.1 \pm 0.3	62.0	6.0 \pm 0.3	3.6
	2 \rightarrow 1	35.3 \pm 0.3	36.5	5.2 \pm 0.3	2.2
	3 \rightarrow 2	24.5 \pm 0.2	25.1	4.8 \pm 0.3	5.7
	3 \rightarrow 0	120.0 \pm 1.5	123.7	9.8 \pm 1.5	8.0
54.5 MeV ^a	1 \rightarrow 0	161.0 \pm 0.5	163.7	20.5 \pm 0.6	10.3
	2 \rightarrow 1	103.8 \pm 0.4	105.7	19.2 \pm 1.0	6.5
	3 \rightarrow 2	78.0 \pm 0.3	79.6	15.6 \pm 0.6	4.9
	4 \rightarrow 3	60.3 \pm 1.5	59.7	11.2 \pm 1.5	8.3
	4 \rightarrow 1	240.2 \pm 1.5	245.0	9.8 \pm 1.5	14.1

^aThese values supersede the ones given in Table 1 of Ref. 3.

Table II. <100> axial transition energies.

Beam energy	Transition	Observed energy (keV)	Calculated energy (keV)
16.9 MeV	3p → 1s	101.5 ± 1.0	100.0
	2p → 1s	58.3 ± 0.5	57.9
	3d → 2p	35.0 ± 0.5	33.9
	several	21.9 ± 1.0	20.5 ^a
30.5 MeV	2p → 1s	161.6 ± 2.0	168.4
	3d → 2p	110.4 ± 1.0	111.4
	4f → 3d	71.2 ± 1.0	72.0
	4d → 3p	52.3 ± 1.5	51.0
	(5g) → 4f	47.4 ± 1.5	46.7
	several	34.1 ± 1.0	35.0 ^b

a Strength-weighted mean of 12 closely-spaced transitions.

b Strength-weighted mean of 10 closely-spaced transitions.

Table III. Defect-corrected planar linewidths.^a

Plane and Beam energy	Transition	Observed energy (keV)	Observed linewidth (keV)	Calculated linewidth 1 (keV)	Calculated linewidth 2 (keV)
(100)					
30.5 MeV	1 → 0	43.0	5.9 ± 0.3	5.5	6.7
54.5 MeV	1 → 0	119.8	18.7 ± 0.7	7.3	15.3
	2 → 1	64.7	23.8 ± 3.0	20.3	23.4
(110)					
16.9 MeV	1 → 0	23.3	3.3 ± 0.4	2.3	2.7
30.5 MeV	1 → 0	60.1	6.0 ± 0.3	3.6	5.8
	2 → 1	35.3	5.2 ± 0.3	2.2	4.4
	3 → 2	24.5	4.8 ± 0.3	5.7	6.7
54.5 MeV	1 → 0	161.0	20.5 ± 0.6	10.3	19.2
	2 → 1	103.8	19.2 ± 1.0	6.5	15.6
	3 → 2	78.0	15.6 ± 0.6	4.9	14.2
	4 → 3	60.3	11.2 ± 1.5	8.3	15.1

^a Calculated linewidth 1 is the standard calculation (as in Sec. II); calculated linewidth 2 takes into account a 0.9-μm defect coherence length.

Table IV. Energy scaling.

(100)		1 → 0		2 → 1		
Electron energy (MeV)	Photon energy (keV)	α	α_{av}	Photon energy (keV)	α	α_{av}
30.5	43.0	1.77 1.80 1.63	1.73	64.7	2.00 1.96	1.98
54.5	119.8			139.2		
80.2	237.2			256.0		
110.2	399.5					

(110)		1 → 0		2 → 1		3 → 2		4 → 3			
Electron energy (MeV)	Photon energy (keV)	α	α_{av}	Photon energy (keV)	α	α_{av}	Photon energy (keV)	α	α_{av}		
16.9	23.3	1.63 1.73 1.73 1.60	1.67	35.3	1.89 1.88 1.73	1.83	24.5	2.03 1.93 1.79	1.92		
30.5	60.1			103.8			78.0				
54.5	161.0			211.7			162.7				
80.2	310.2			370			290				
110.2	520					235					
							60.3			2.00 1.85	1.93
							128.8				
							235				

<100>		2p → 1s		3d → 2p		
Electron energy (MeV)	Photon energy (keV)	α	α_{av}	Photon energy (keV)	α	α_{av}
4.0	3.80	2.02 1.76	1.89	35.0	1.98	1.98
16.9	58.3			110.4		
30.5	161.6					

FIGURE CAPTIONS

Fig. 1(a) The reciprocal lattice vectors used in a 3x3-beam $\langle 100 \rangle$ calculation.

(b) The reciprocal lattice vectors used in a 9-beam (100) calculation, illustrating how the reciprocal lattice vectors of the planar calculation reach much farther into the reciprocal lattice than those of an axial calculation equivalent in size.

Fig. 2(a) The $\langle 100 \rangle$ potential calculated for several different numbers of beams.

(b) The (100) potential calculated for several different numbers of beams. Note that the (100) potential can be determined accurately using only 13 terms, while the $\langle 100 \rangle$ potential requires more than 121 terms.

Fig. 3 The wave functions $\chi(x) = (\chi^* \chi)^{1/2}$ with $k = 0$ for the first three bound states of (110) diamond for an incident electron energy of 16.9 MeV. Note the alternating parity of the wave functions.

Fig. 4 Schematic diagram (not to scale) of the experimental arrangement at the Livermore linac for the measurement of channeling-radiation spectra from positrons or electrons (see text).

Fig. 5 Schematic diagram (not to scale) of the experimental arrangement at the Livermore linac for the measurement of the transmission of positrons or electrons through a crystal (see text).

- Fig. 6 Tilt-angle scans near the (100) plane of a 17.4- μm -thick silicon crystal, using (a) the transmission of 56-MeV positrons and (b) the radiation from 54-MeV electrons (note the expanded angular scale).
- Fig. 7 Map of the silicon crystal constructed from planar scans such as the one shown in Fig. 5(a). The planes intersect at the $\langle 110 \rangle$ axis.
- Fig. 8 Transmission scans through the $\langle 110 \rangle$ axis of the silicon crystal whose map is shown in Fig. 6(a) for 56-MeV positrons and (b) for 56-MeV electrons.
- Fig. 9 Block diagram of the data-collection electronics (see text).
- Fig. 10 Raw (100) data spectrum with random spectrum below it for 54.5-MeV electrons. Both spectra are for the same amount of beam flux.
- Fig. 11 Least-squares curve fit to the random-subtracted (100) spectrum of Fig. 10. Lorentzian peaks and a second-order polynomial background are fitted to the data (see text).
- Fig. 12(a) The (100) potential and eigenvalues for 16.9-MeV electrons.
(b) The (100) spectrum for 16.9 MeV.
(c) The (100) potential and eigenvalues for 30.5-MeV electrons.
(d) The (100) spectrum for 30.5 MeV.
(e) The (100) potential and eigenvalues for 54.5-MeV electrons.

(f) The (100) spectrum for 54.5 MeV.

In this and subsequent figures, all of the spectra shown are random-subtracted. The vertical lines in the spectra indicate the energies and relative intensities of the calculated transitions, assuming equal initial level populations. The counting-rate units are the same for all spectra obtained at the same energy.

Fig. 13(a) The (110) potential and eigenvalues for 16.9-MeV electrons.

(b) The (110) spectrum for 16.9 MeV.

(c) The (110) potential and eigenvalues for 30.5-MeV electrons.

(d) The (110) spectrum for 30.5 MeV.

(e) The (110) potential and eigenvalues for 54.5-MeV electrons.

(f) The (110) spectrum for 54.5 MeV.

Note the increase with beam energy of the line energies and linewidths.

Fig. 14(a) The (111) potential and eigenvalues for 30.5-MeV electrons.

(b) The (111) spectrum for 30.5 MeV.

(c) The (111) potential and eigenvalues for 54.5-MeV electrons.

(d) The (111) spectrum for 54.5 MeV.

Fig. 15 The (111) spectra for (a) 30.5-MeV electrons and (b) 54.5-MeV electrons. The solid curves are spectra constructed from the calculated transition energies, strengths, and linewidths. The dashed curves are the same as the solid curves, but with the linewidth of each spectral line arbitrarily increased in order to smooth out the predicted spectral shape (see text). Note the

significant difference, for both cases, between the energy of the maximum value of the dashed curve and that of the data.

Fig. 16(a) The $\langle 100 \rangle$ potential and eigenvalues for 16.9-MeV electrons.

(b) The $\langle 100 \rangle$ spectrum for 16.9 MeV.

(c) The $\langle 100 \rangle$ potential and eigenvalues for 30.5-MeV electrons.

(d) The $\langle 100 \rangle$ spectrum for 30.5 MeV.

(e) The $\langle 100 \rangle$ potential and eigenvalues for 54.5-MeV electrons.

(f) The $\langle 100 \rangle$ spectrum for 54.5 MeV.

Bloch-wave broadening for the energy levels is not shown in parts (a), (c), and (e).

Fig. 17(a) The (111A) potential based upon experimental corrections to x-ray and electron scattering factors (light solid curve), together with the eigenvalues for 30.5-MeV electrons. The standard (111) potential, as in Fig. 14(a), is shown as the dashed curve.

(b) The (111) spectrum for 30.5-MeV electrons, together with the calculated spectra obtained from the standard (dashed curve) and (111A) (light solid curve) potentials. The linewidths have been corrected for defect effects (see text).

(c) The (111) spectrum for 54.5-MeV electrons, together with the calculated spectra obtained from the standard (dashed curve) and (111A) (light solid curve) potentials. The linewidths have been corrected for defect effects.

Fig. 18(a) Empirical (111B) potential based upon the best fit to the 30.5-MeV data (heavy solid curve), together with the corresponding

eigenvalues; the standard (111) potential (dashed curve) as in Fig. 14(a); and the (111A) potential based upon experimental x-ray-diffraction data (light solid curve), as shown in Fig. 17(a).

- (b) The (111) spectrum for 30.5-MeV electrons, together with the calculated spectra obtained from the (111B) potential (heavy solid curve) and from the (111A) potential (light solid curve). The linewidths have been corrected for defect effects.
- (c) The (111) spectrum for 54.5-MeV electrons, together with the calculated spectra obtained from the (111B) potential (heavy curve) and from the (111A) potential (light solid curve). The linewidths have been corrected for defect effects.

Fig. 19 The probability densities $\chi(x)^*\chi(x)$ for the bound states of the (110) planar potential for all three incident electron energies, with $k = 0.5$. Note that the wave functions draw in closer to the planes as the electron-beam energy increases.

Fig. 20 The scaling of photon energy vs. electron-beam energy, the latter plotted in units of γ . A denotes the (110) $1 \rightarrow 0$ transition (average $\alpha = 1.67$); B, the (100) $1 \rightarrow 0$ transition (average $\alpha = 1.73$); C, the (110) $2 \rightarrow 1$ transition (average $\alpha = 1.83$); D, the (110) $3 \rightarrow 2$ transition (average $\alpha = 1.92$); E, the (100) $2 \rightarrow 1$ transition (average $\alpha = 1.98$); and F, the (110) $4 \rightarrow 3$ transition (average $\alpha = 1.93$).

Fig. 21 Calculated synthetic spectra for channeling radiation from 30.5-MeV electrons along the (100) direction in diamond at room temperature (solid curve) and at 810°C (dashed curve).

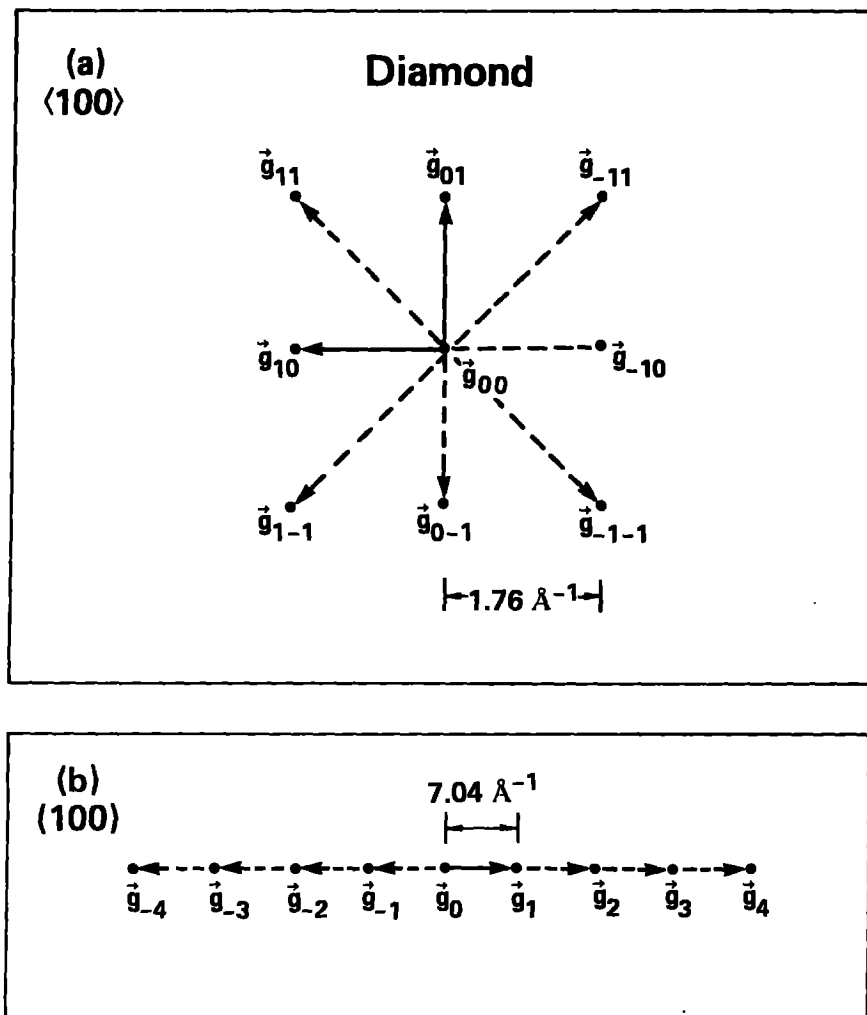


Figure 1

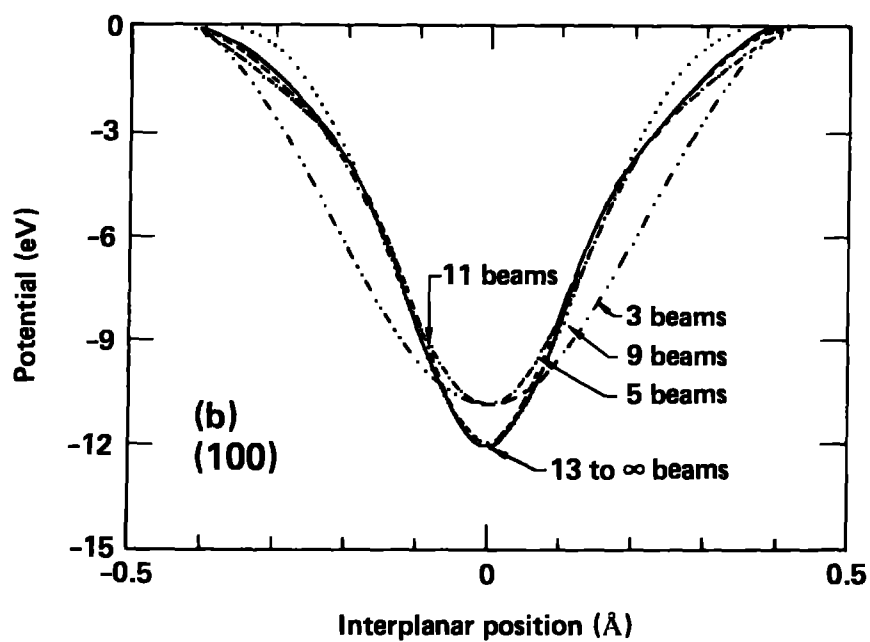
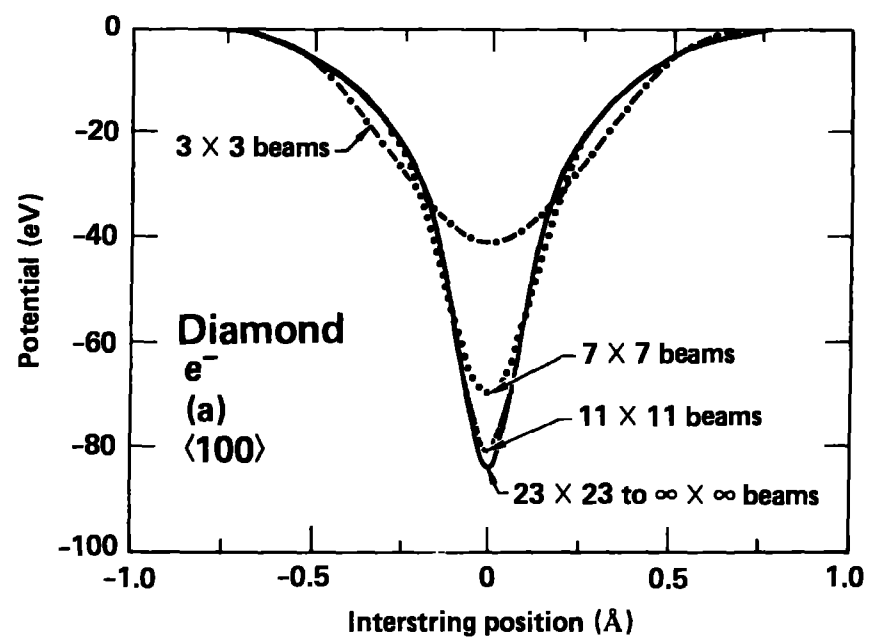


Figure 2

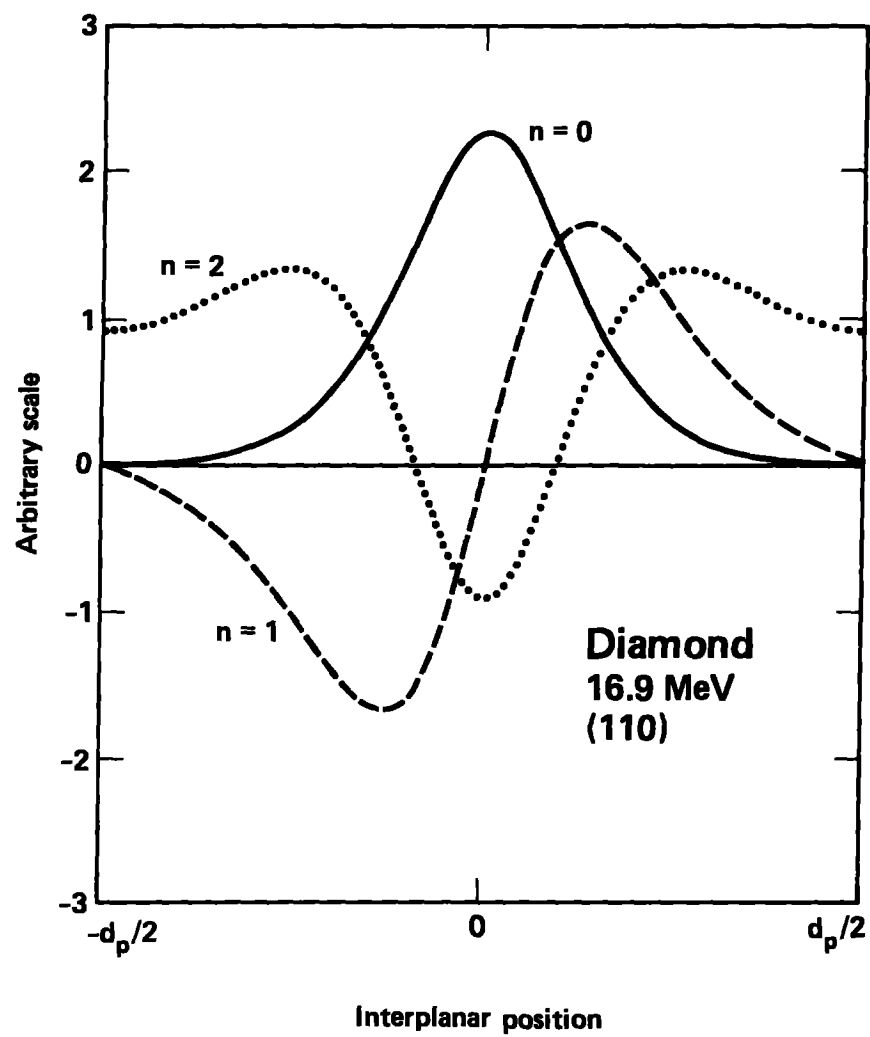


Figure 3

Radiation

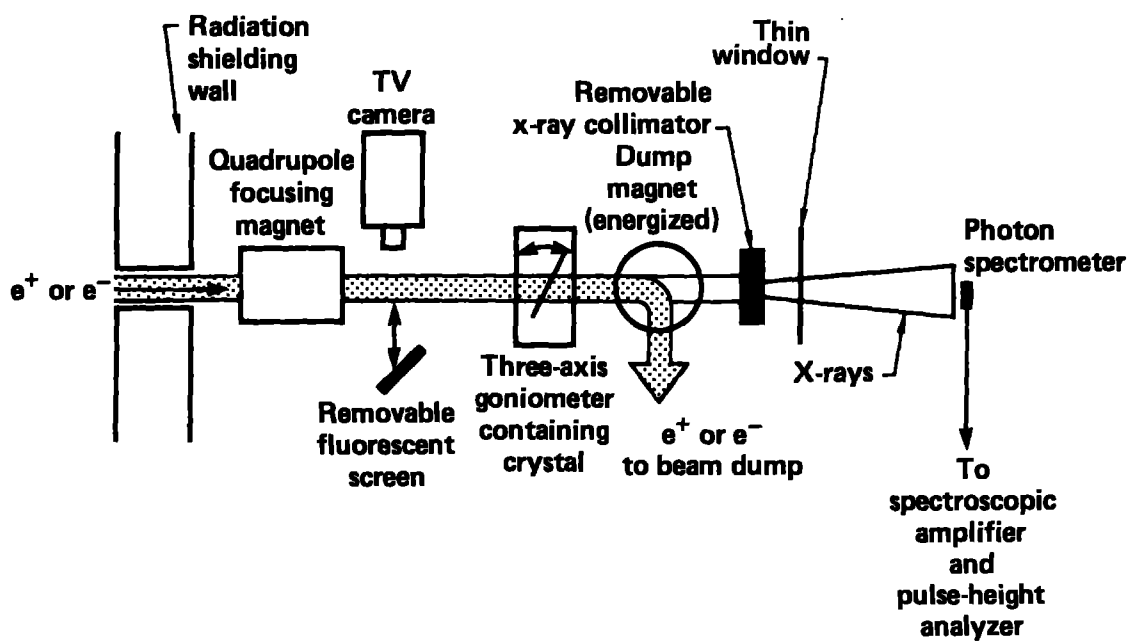


Figure 4

Transmission

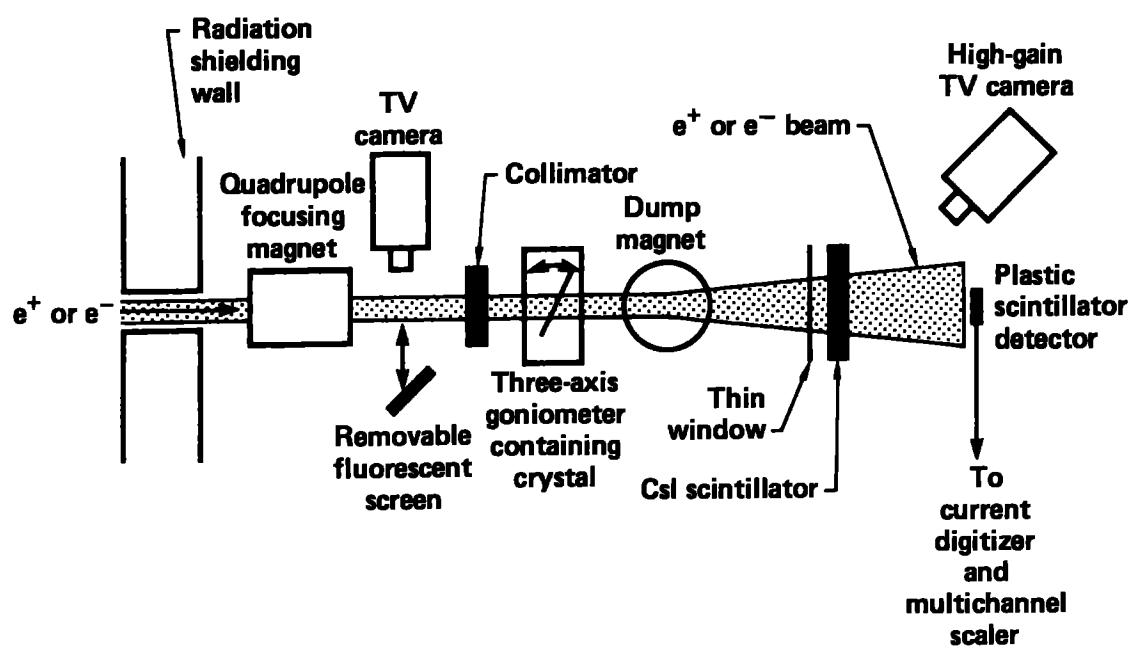


Figure 5

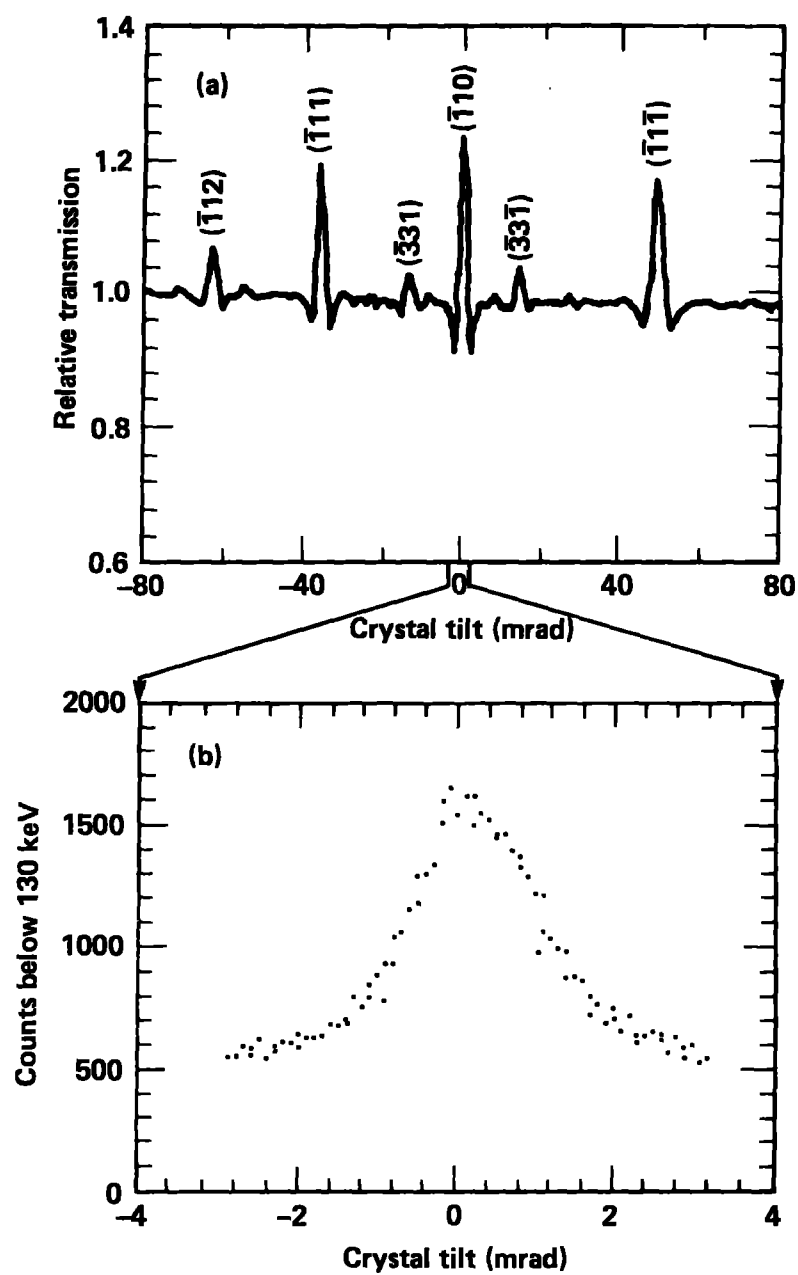


Figure 6

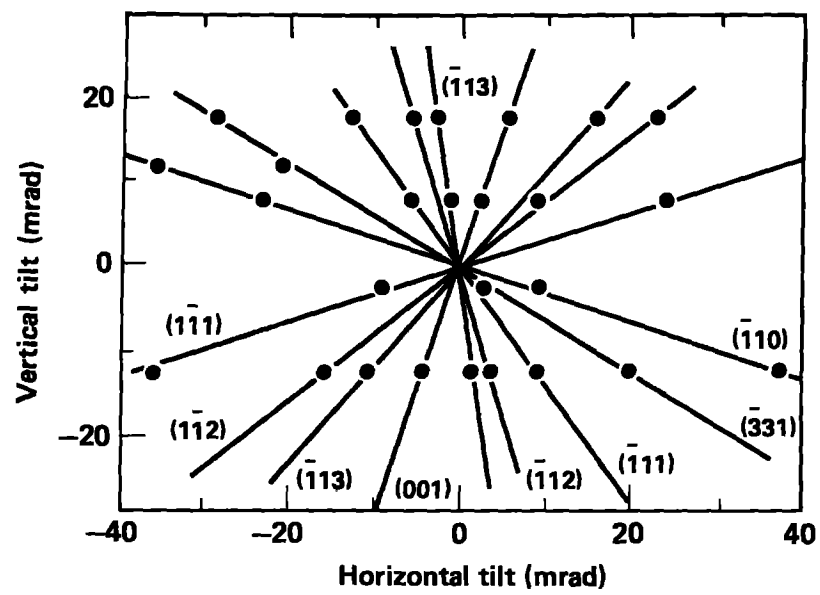


Figure 7

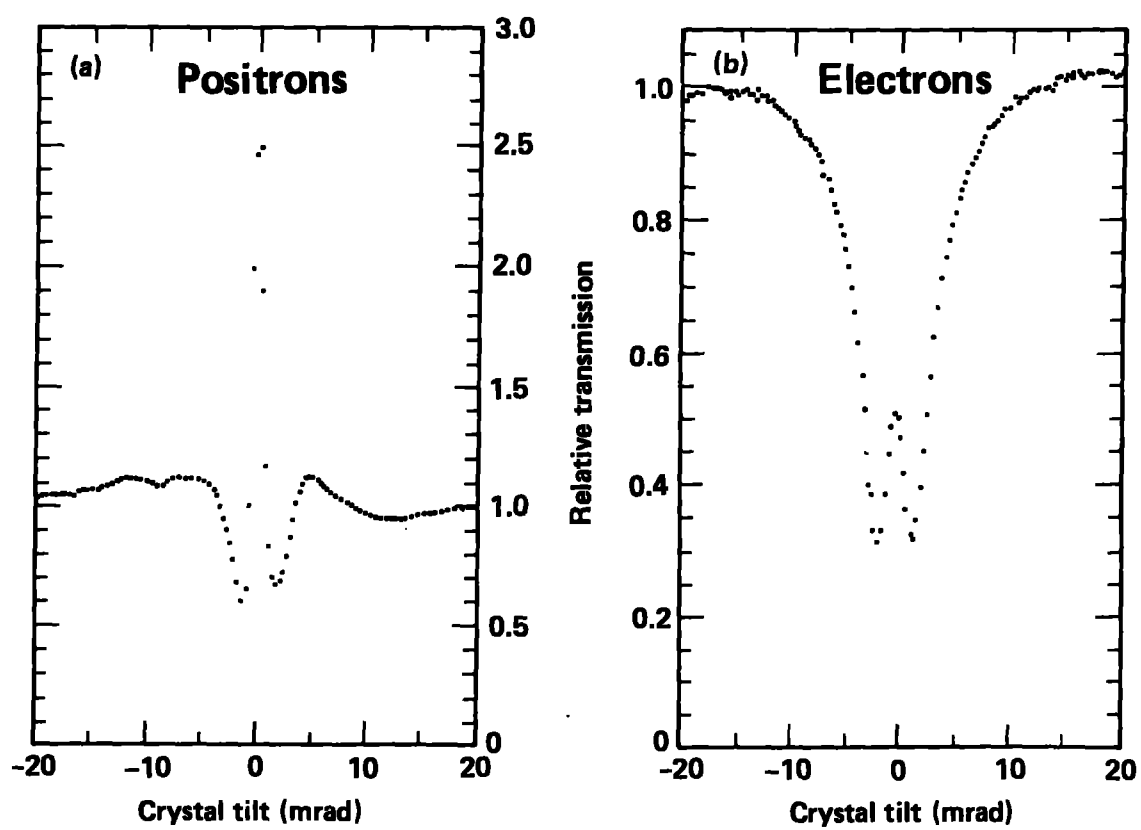


Figure 8

Data-Collection Electronics

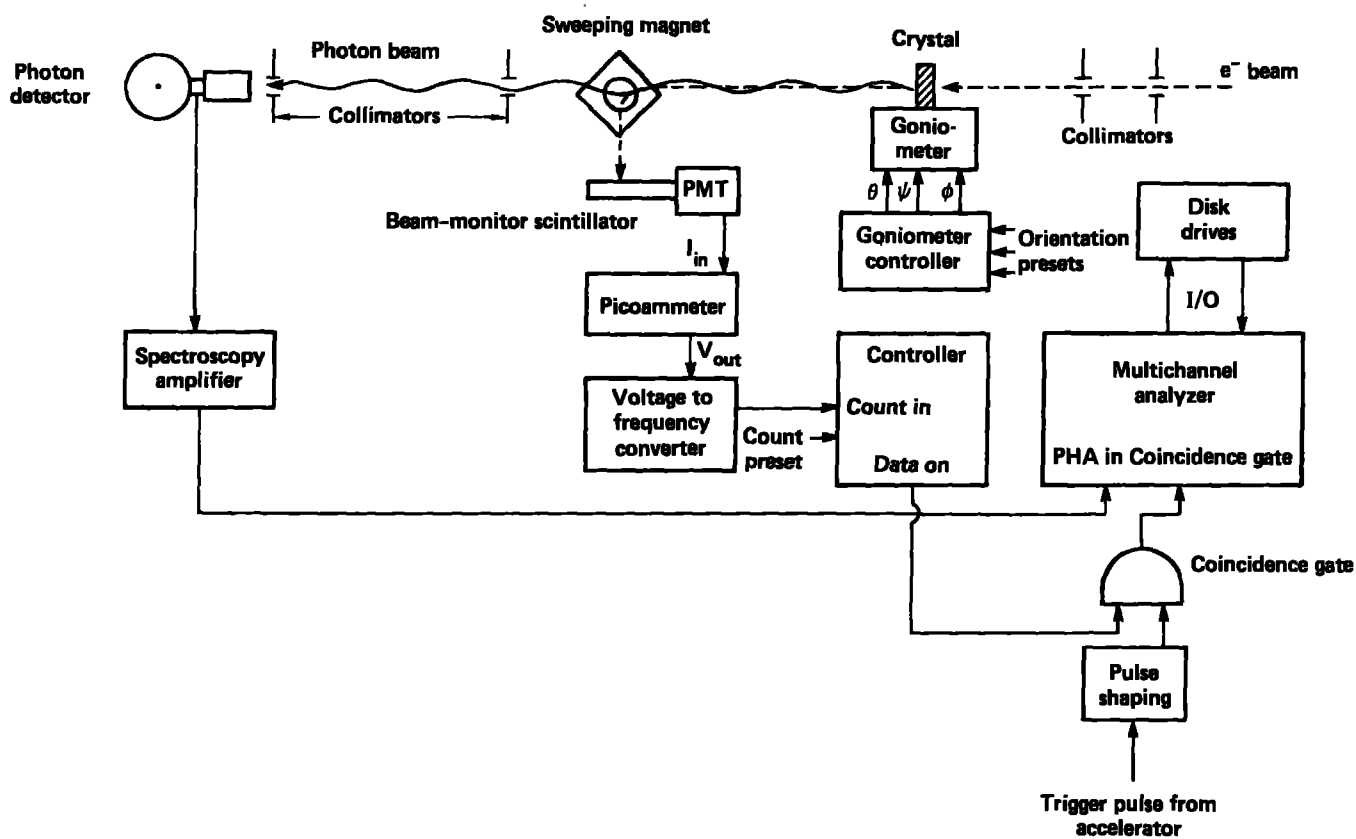


Figure 9

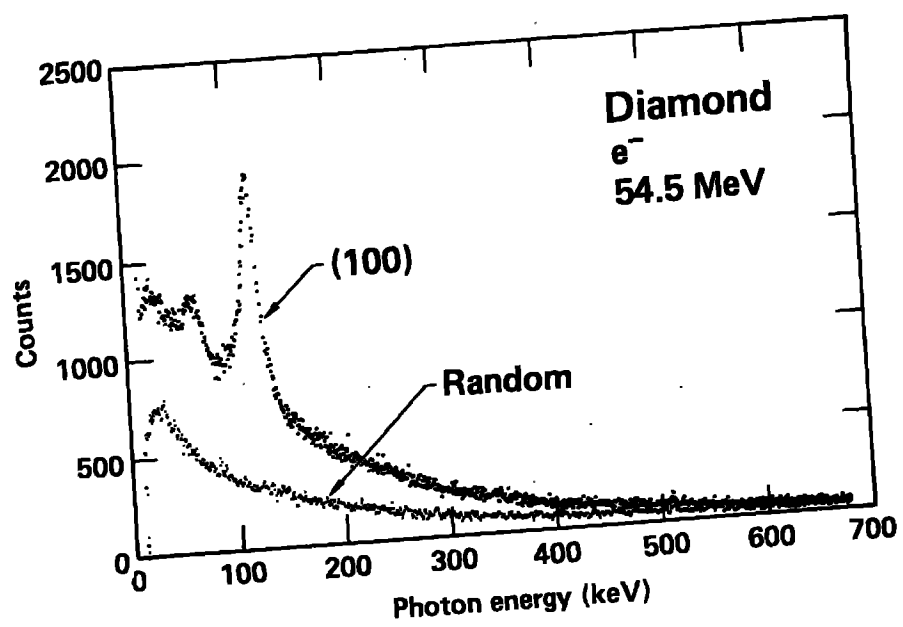


Figure 10

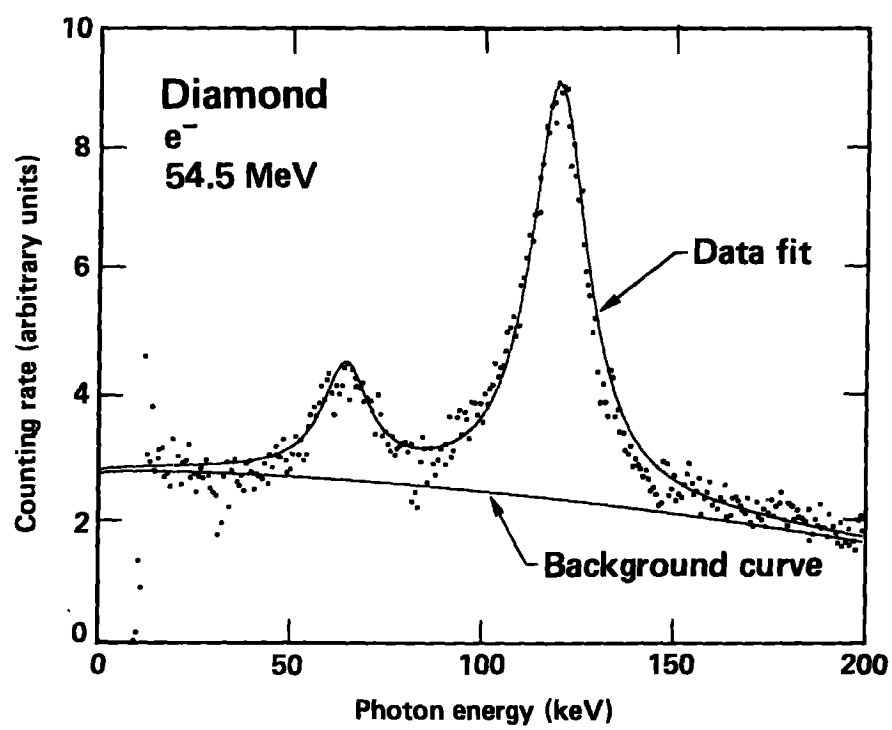


Figure 11

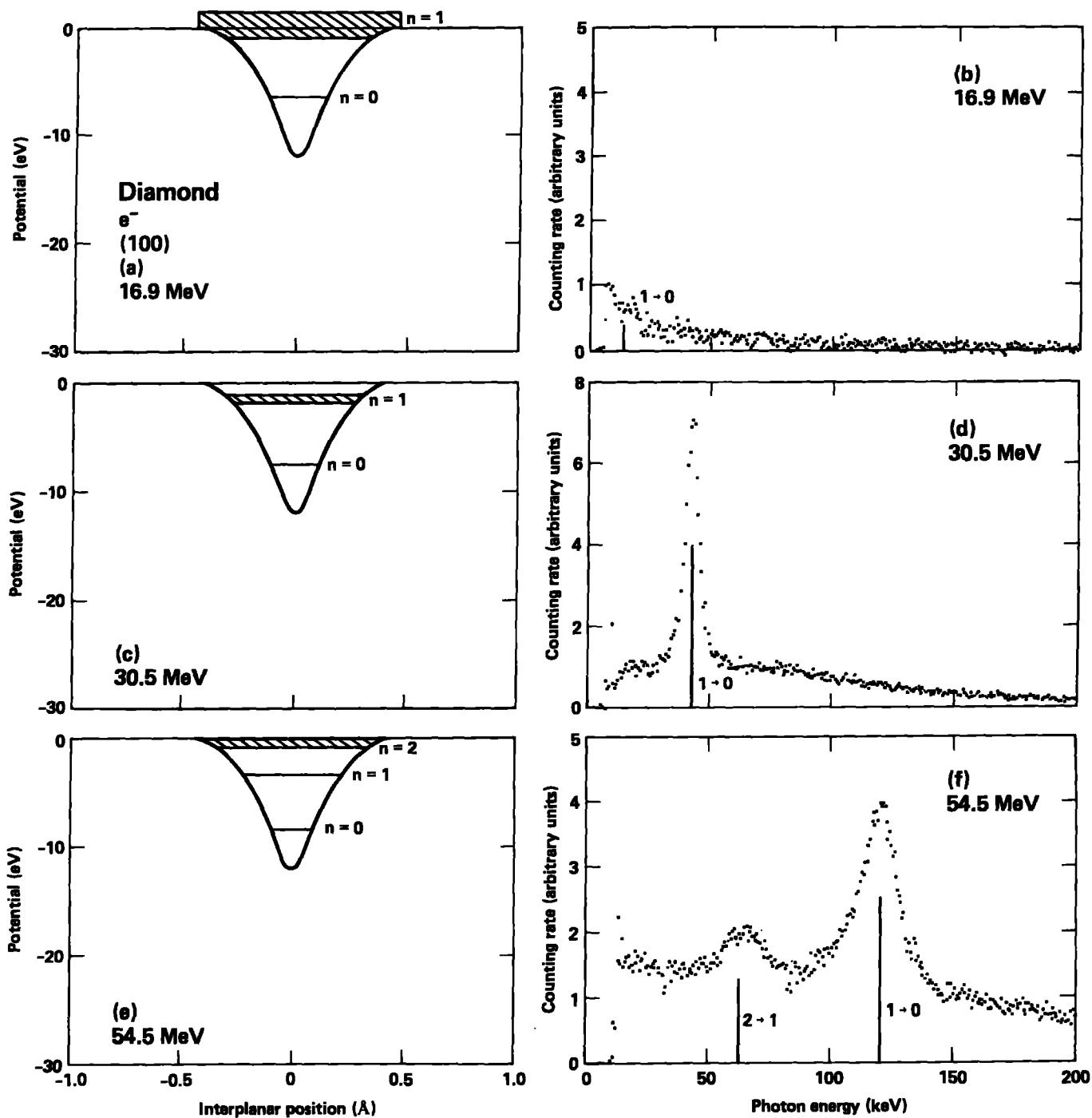


Figure 12

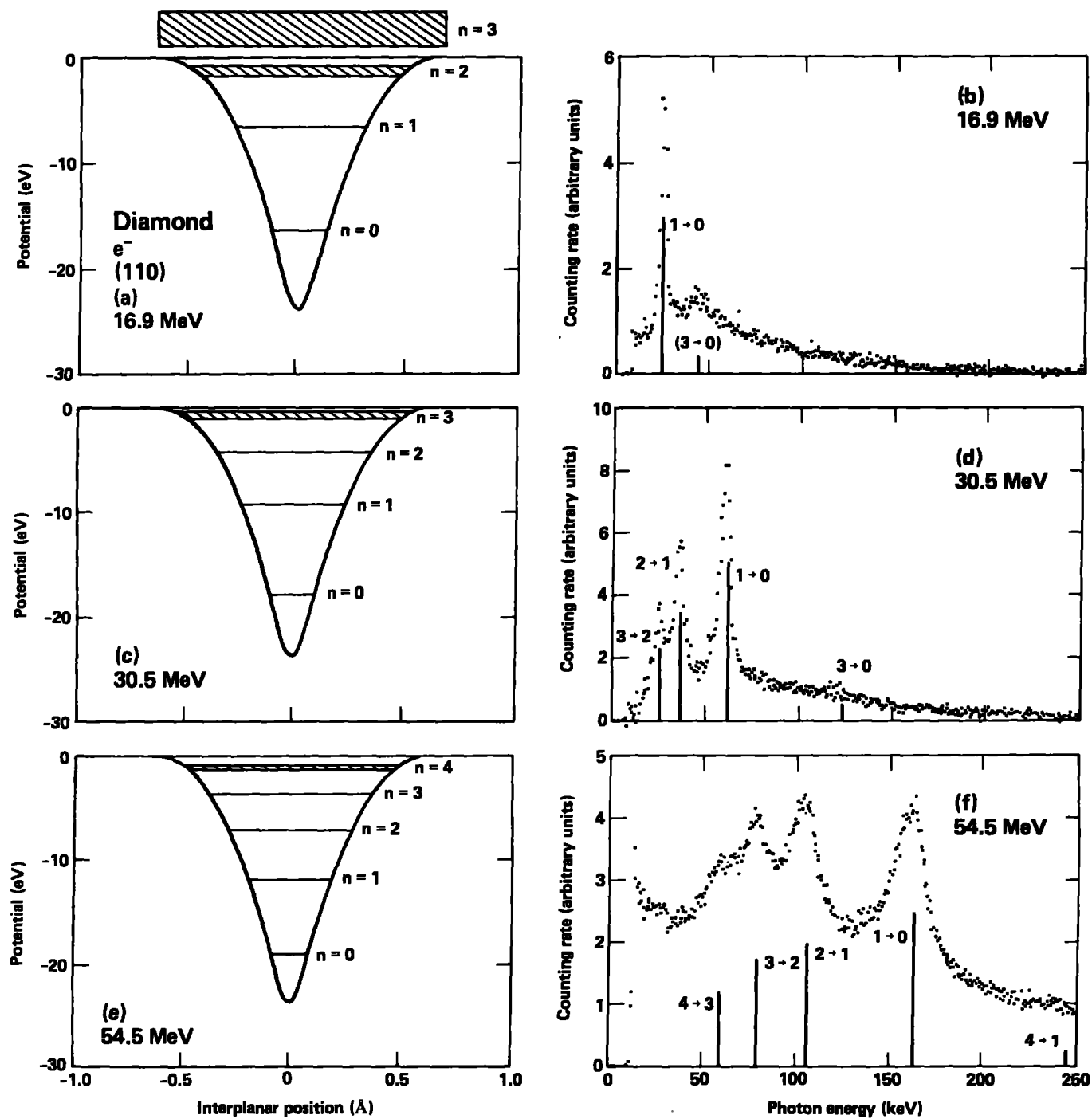


Figure 13

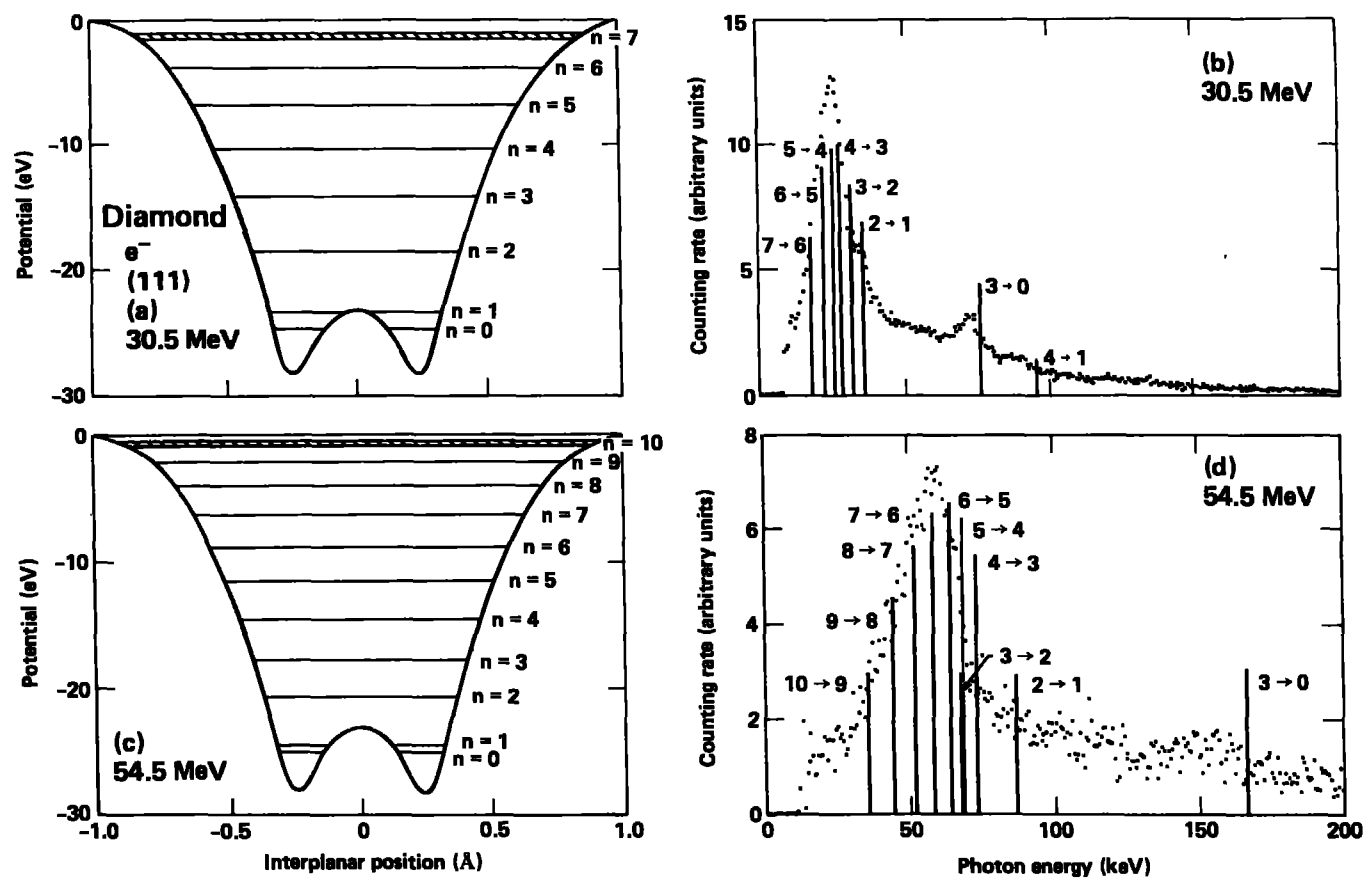


Figure 14

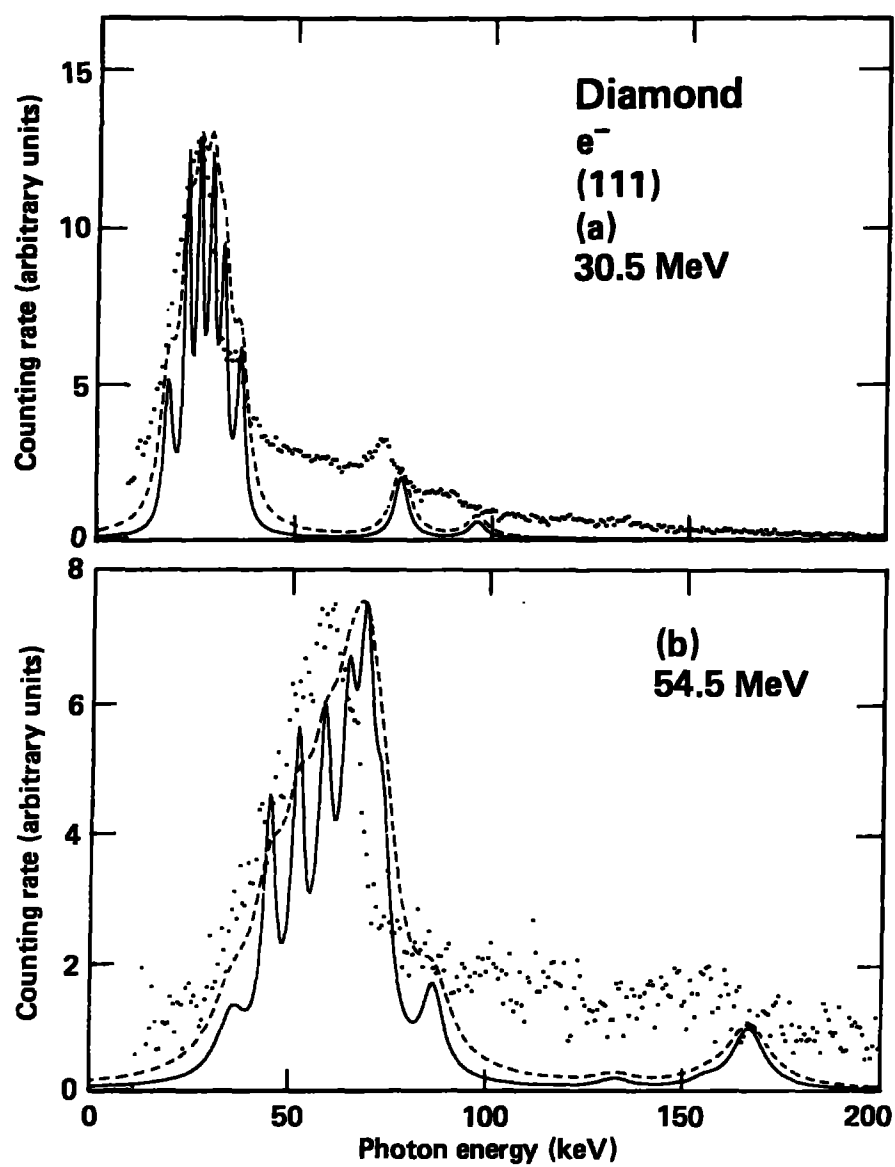


Figure 15

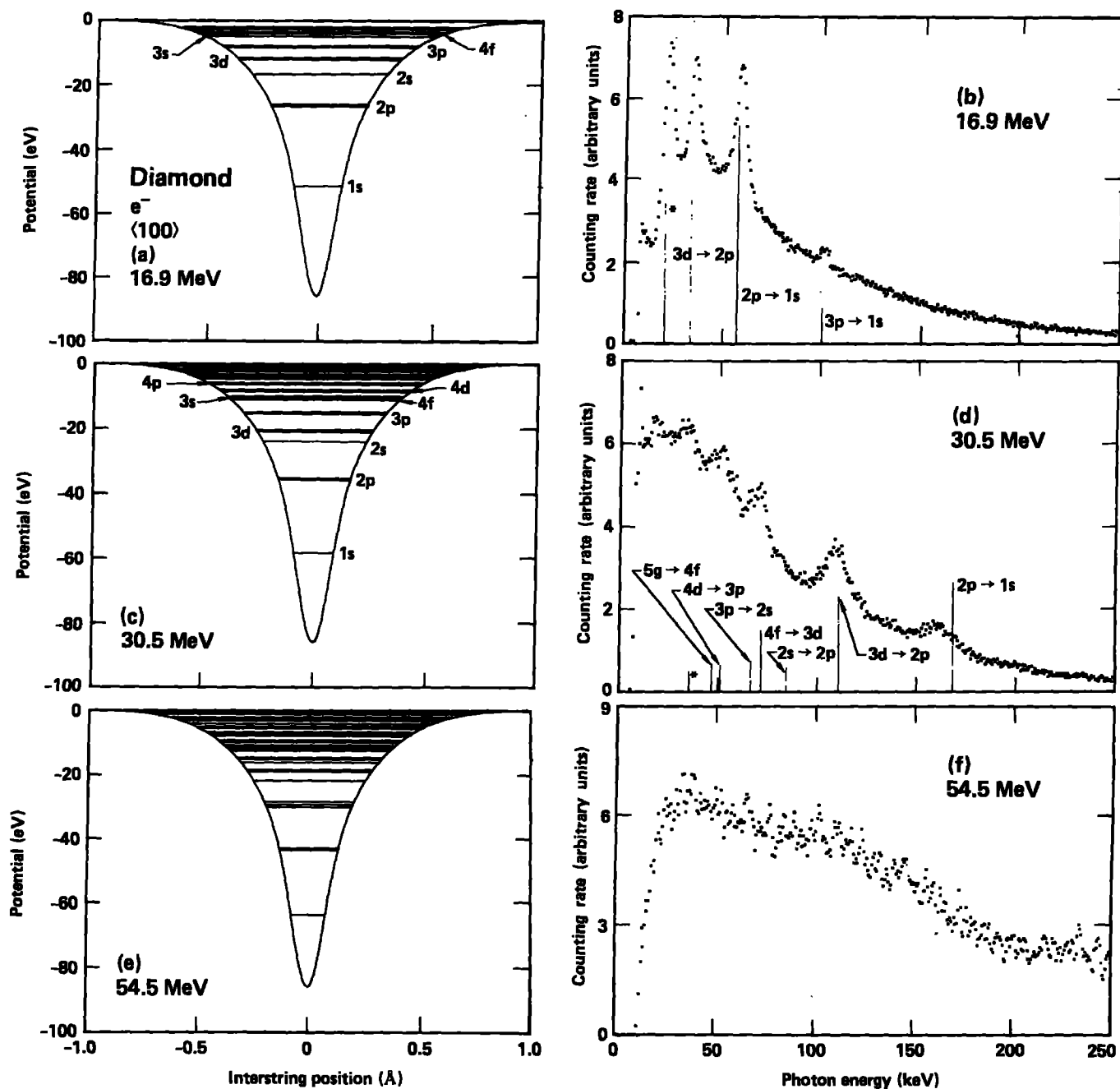


Figure 16

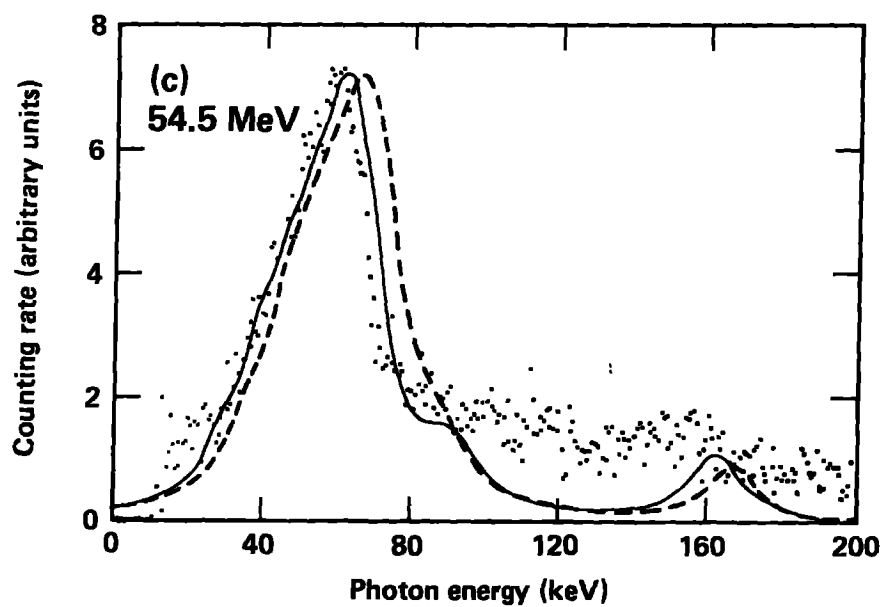
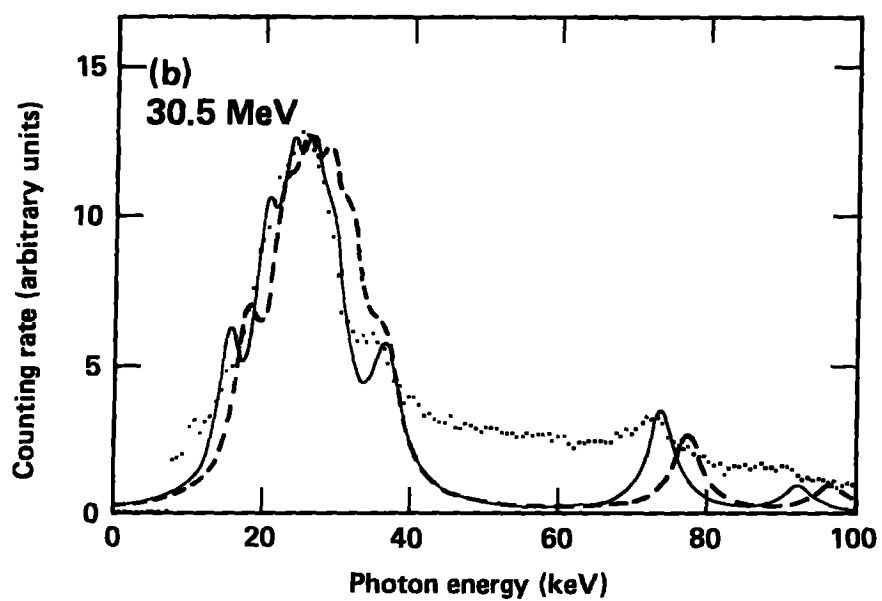
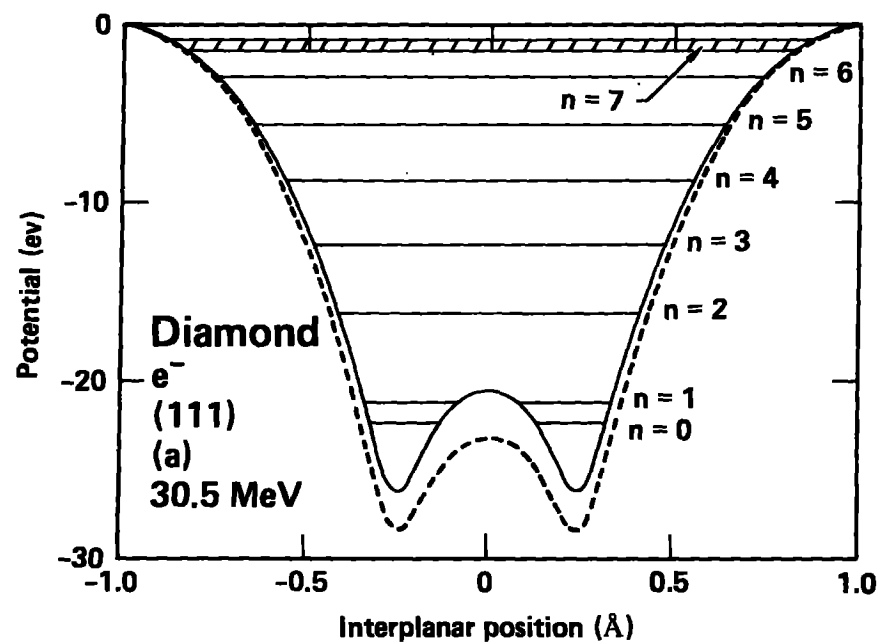


Figure 17

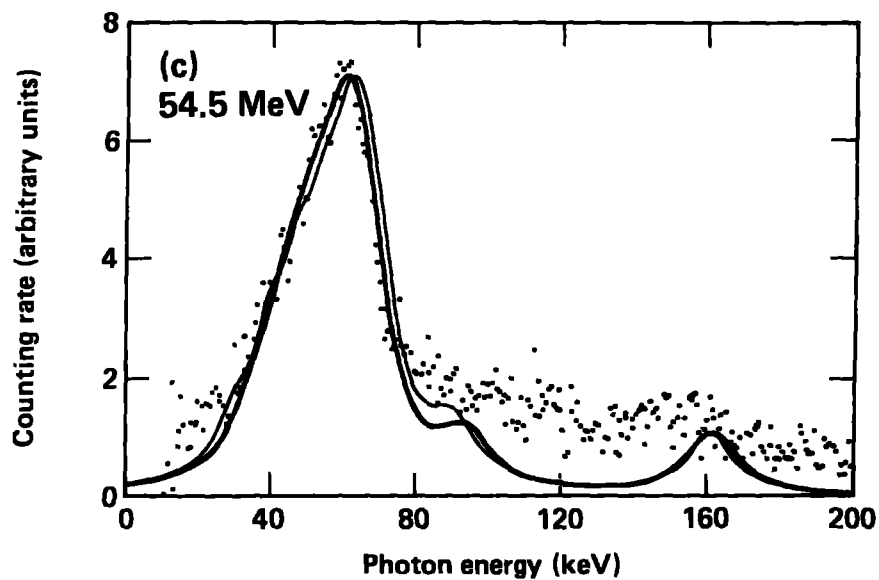
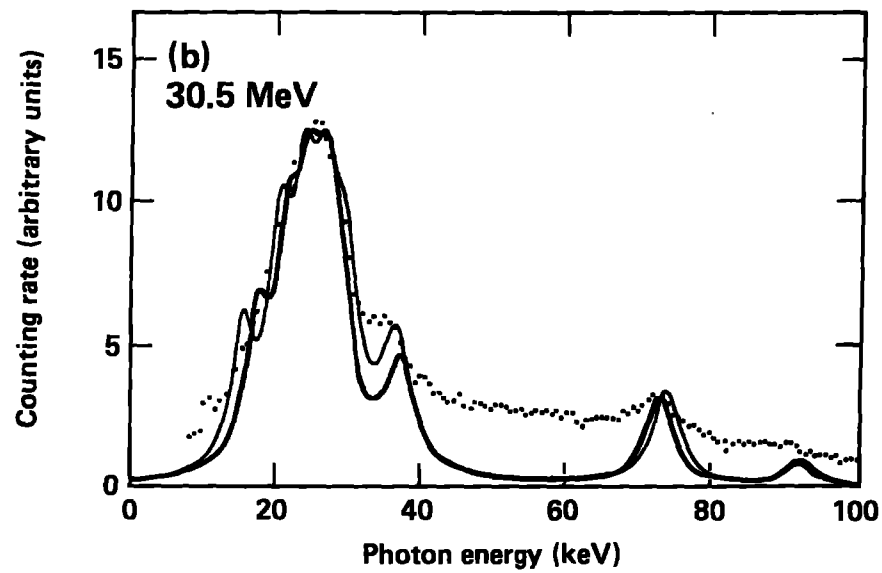
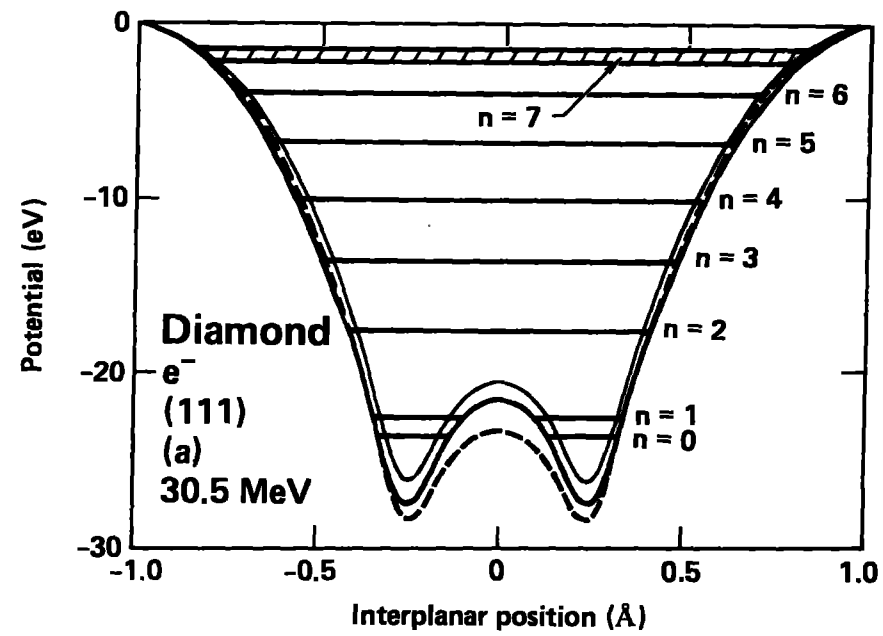


Figure 18

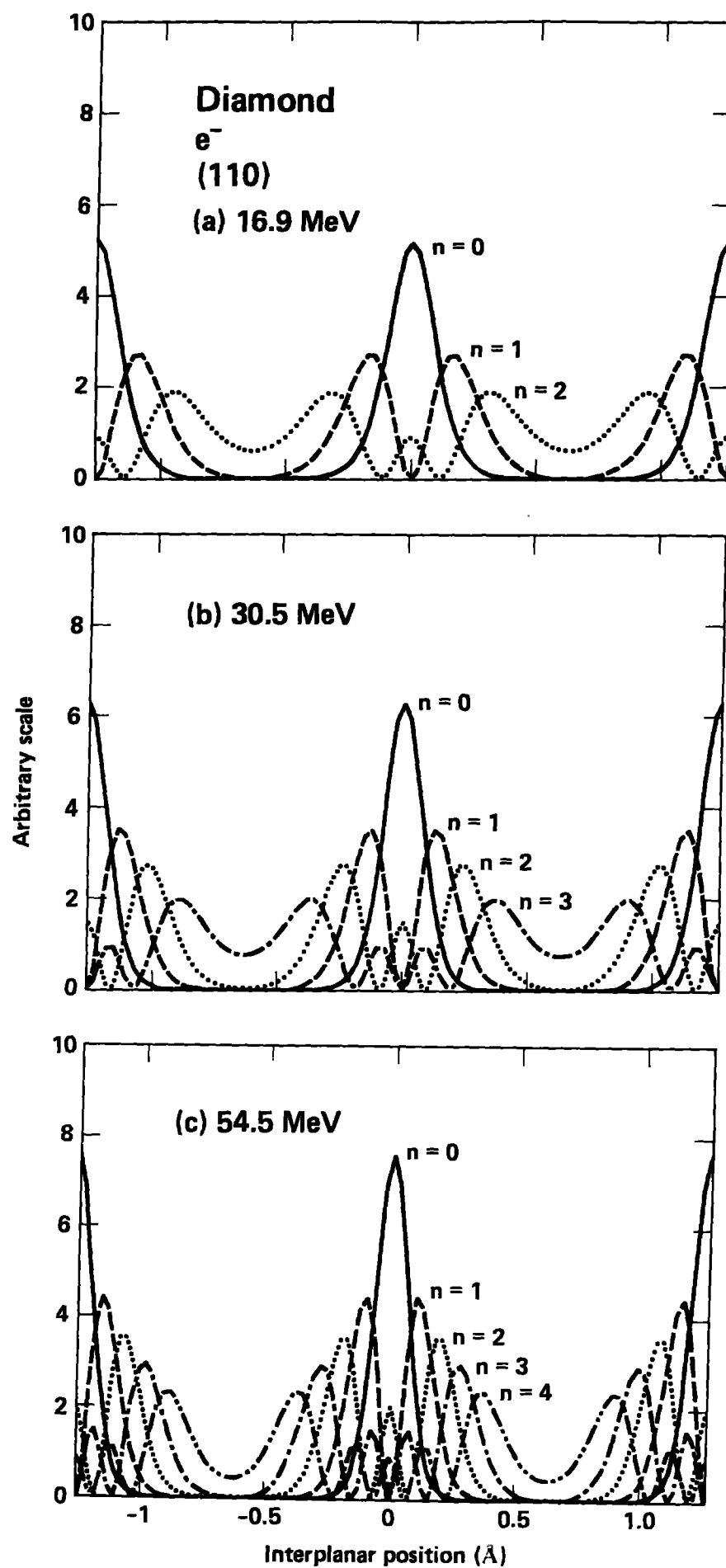


Figure 19

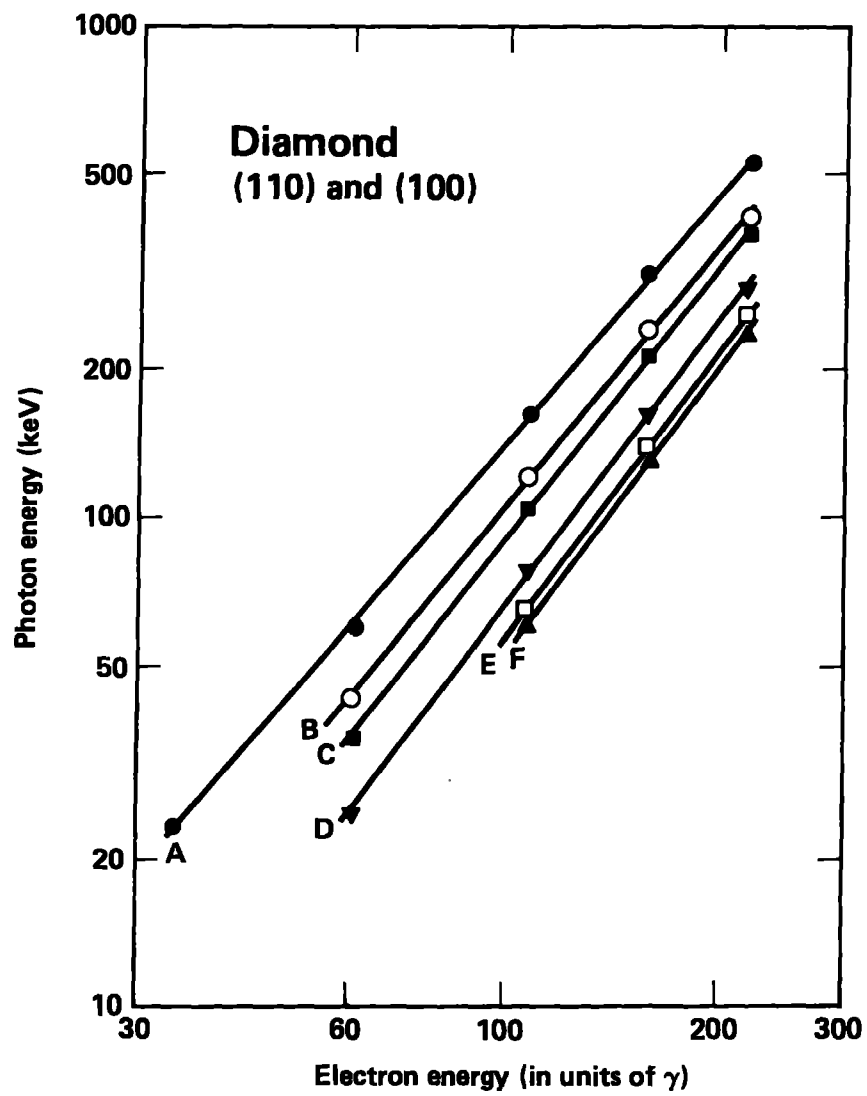


Figure 20

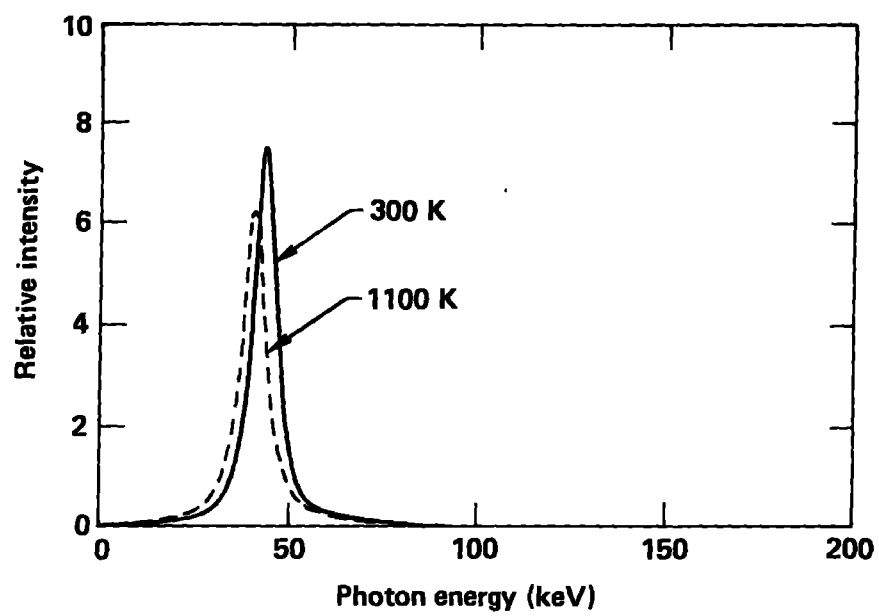


Figure 21